Plasmonics (2025) 20:3161–3184
https://doi.org/10.1007/s11468-024-02489-w

RESEARCH

Nanoengineered Graphene Metasurface Surface Plasmon Resonance Sensor for Precise Hemoglobin Detection with AI-Assisted Performance Prediction

Jacob Wekalao[1] · **Ngaira Mandela**[2] · **Obed Apochi**[3] · **Costable Lefu**[4] · **Tobias Topisia**[5]

Received: 30 June 2024 / Accepted: 11 August 2024 / Published online: 13 September 2024
© The Author(s), under exclusive licence to Springer Science+Business Media, LLC, part of Springer Nature 2024

Abstract

The development of highly sensitive and reliable biosensors for hemoglobin detection is crucial for various medical and diagnostic applications. Hemoglobin, a vital protein in red blood cells responsible for oxygen transport, serves as an important biomarker for numerous health conditions. Accurate and rapid measurement of hemoglobin levels can aid in the early detection and monitoring of anemia, blood disorders, and other medical conditions. This study presents a biosensor design for hemoglobin detection, integrating a graphene-based metasurface with circular and square ring resonators constructed from silver and gold nanostructures. The proposed sensor leverages the unique plasmonic properties of plasmonic nanostructures and the remarkable optical characteristics of graphene to enhance its performance. Extensive parametric analysis and optimization are conducted to enhance detection accuracy among other performance parameters. Detection analysis demonstrated the sensor's ability to resolve changes in hemoglobin concentration through distinct shifts in transmittance and reflectance spectra. The resulting sensor exhibits enhanced sensitivity of 3500nmRIU^{-1} to infrared energy, maximum FOM of 17.6, and detection limits of 0.05 among other performance parameters. Furthermore, machine learning optimization using 1D convolutional neural network regression is employed to predict the sensor's behavior achieving high accuracy with maximum R^2 scores ranging up to 1. The sensor design exhibits remarkable potential for applications requiring highly sensitive and precise hemoglobin monitoring in medical diagnostics and healthcare.

Keywords Optical sensing · Artificial intelligence · Nanophotonics · Metasurface · Graphene

Introduction

Hemoglobin is an essential protein in red blood cells that facilitates oxygen transport throughout the body [1]. Precise detection of hemoglobin is vital for diagnosing and tracking numerous health conditions, such as anemia, hemoglobinopathies, and cardiovascular diseases [2]. The development of sensitive and selective hemoglobin sensors poses a major challenge in healthcare applications [3]. Traditional methods frequently involve complex procedures, lack specificity, or have limited sensitivity, which impedes timely and accurate diagnosis [4, 5].

Biosensors are devices that integrate a biological element with a physicochemical detector to identify, capture, and convey data related to biochemical processes [6]. These devices have transformed various areas such as medicine, environmental monitoring, food security, and biodefense, by offering swift, precise, and economical identification and assessment of biological molecules,

✉ Jacob Wekalao
jacob.phdfs2303@nfsu.ac.in

[1] School of Engineering and Technology, National Forensic Sciences University, Gandhinagar 382007, Gujarat, India

[2] School of Digital Forensics and Cyber Security, National Forensic Sciences University, Gandhinagar 382007, Gujarat, India

[3] School of Behavioral Sciences, National Forensic Sciences University, Gandhinagar 382007, Gujarat, India

[4] School of Pharmacy, National Forensic Sciences University, Gandhinagar 382007, Gujarat, India

[5] School of Forensic Sciences, National Forensic Sciences University, Gandhinagar 382007, Gujarat, India

cells, and microorganisms [7–9]. The biological components of biosensors can be an enzyme, antibody, nucleic acid, cell, or tissue, selected for its specificity and affinity towards the target analyte [10]. This component interacts with the analyte, triggering a biochemical reaction that produces a measurable signal [11]. The physicochemical detector component, such as an electrochemical, optical, or mass-based transducer, then converts this signal into an electrical or optical output that can be quantified and analyzed [12].

Optical sensors are pivotal in modern technology across various fields, harnessing the principles of light to operate [13]. These sensors use different forms of light like visible, infrared, ultraviolet, or even laser beams to collect data about specific targets [14]. Optical sensors function by using the interaction between light and matter. They can detect variations in light intensity, wavelength, polarization, and phase, converting these changes into measurable electrical signals [15]. The essential components generally consist of a light source, such as an LED or laser, and a photodetector that transforms light into an electrical signal [16].

Graphene, gold, and silver nanostructures have unique optical and plasmonic properties, which are critical for various applications. Graphene has high transparency and significant light absorption across the UV–visible-NIR spectrum [17]. It also supports surface plasmon resonances, which can be tuned via doping or electrostatic gating, making it highly useful in sensors and optoelectronic devices [18, 19]. Graphene and its derivatives are known for their significant fluorescence quenching properties, where fluorescent molecules or quantum dots near graphene undergo efficient non-radiative energy transfer, thus reducing fluorescence [20].

Gold nanoparticles (AuNPs) exhibit localized surface plasmon resonance (LSPR), which enhances light absorption and scattering at specific wavelengths due to the collective oscillation of conduction electrons [21]. These properties render AuNPs ideal for applications in biological sensing, imaging techniques such as surface-enhanced Raman scattering (SERS), and photothermal therapy [22]. Similarly, silver nanoparticles (AgNPs) show strong LSPR within the visible spectrum, which can be precisely adjusted by altering the nanoparticle size and shape [23]. With a higher extinction coefficient than gold, AgNPs effectively enhance local electromagnetic fields and amplify signals in sensing applications [24].

Surface-enhanced Raman scattering (SERS) employs plasmonic properties of nanostructures to amplify the Raman scattering signal of molecules adsorbed on their surfaces [25]. This technique provides high sensitivity and selectivity, making it essential in biosensing by enabling the detection of trace biomolecules, such as proteins and DNA, and allowing for the multiplexed detection of multiple analytes simultaneously [26].

Traditional hemoglobin detection methods often involve invasive blood draws and time-consuming laboratory analysis. There is a growing need for non-invasive, real-time, and highly sensitive hemoglobin sensors that can provide quick and accurate results. This study presents an advanced approach to hemoglobin detection through the design and analysis of a graphene-based metasurface sensor. By integrating the unique properties of graphene with noble metal nanostructures, we aim to develop a highly sensitive and tunable platform for hemoglobin sensing. The proposed sensor design leverages the exceptional optical and electronic properties of graphene, combined with the plasmonic characteristics of silver and gold nanostructures, to enhance detection capabilities. Furthermore, the integration of artificial intelligence using 1D convolutional neural network regression is aimed to increase the accuracy of the results and reduce the simulation time as well as resources.

Design and Modeling

The sensor design adopts a straightforward approach, using graphene as a key component. It features two distinct resonator shapes: a square and a circular configuration, both positioned on a graphene layer. The sensor's foundation is a SiO_2 substrate, which includes a ground plane back reflector. The substrate is square-shaped, with dimensions of 4 µm. The circular ring resonator is coated with silver. This resonator has an inner radius of 1 µm and an outer radius of 1.2 µm, with a SiO_2 layer beneath it measuring 0.8 µm in thickness. The sensor design is optimized for effective interaction with incoming infrared radiation. A layer of graphene is applied to the square resonator. Infrared radiation from an external source interacts with the plasmonic materials, generating specific resonance peaks that are captured by an infrared detector. This process is fundamental to the sensor's operation. The square resonator measures 3 µm and 3.5 µm. The sensor's design is comprehensively illustrated in Fig. 1a, c, which presents the layout from three views: a 3D perspective, a top-down view, and a frontal cross-section.

Fabrication Feasibility of the Proposed Sensor Design

To fabricate the sensor, a silicon wafer is chosen as the base material and cleaned thoroughly to remove any contaminants. Next, a layer of SiO_2 is grown on the silicon wafer through thermal oxidation, serving as the substrate for subsequent depositions. A metal layer (typically aluminum or silver) is then deposited onto the SiO_2 layer to act as the ground plane back reflector, enhancing reflection efficiency. Following this, graphene is grown on top of the SiO_2 substrate and metal reflector using chemical vapor deposition (CVD). This method is known for producing high-quality graphene films (Fig. 2).

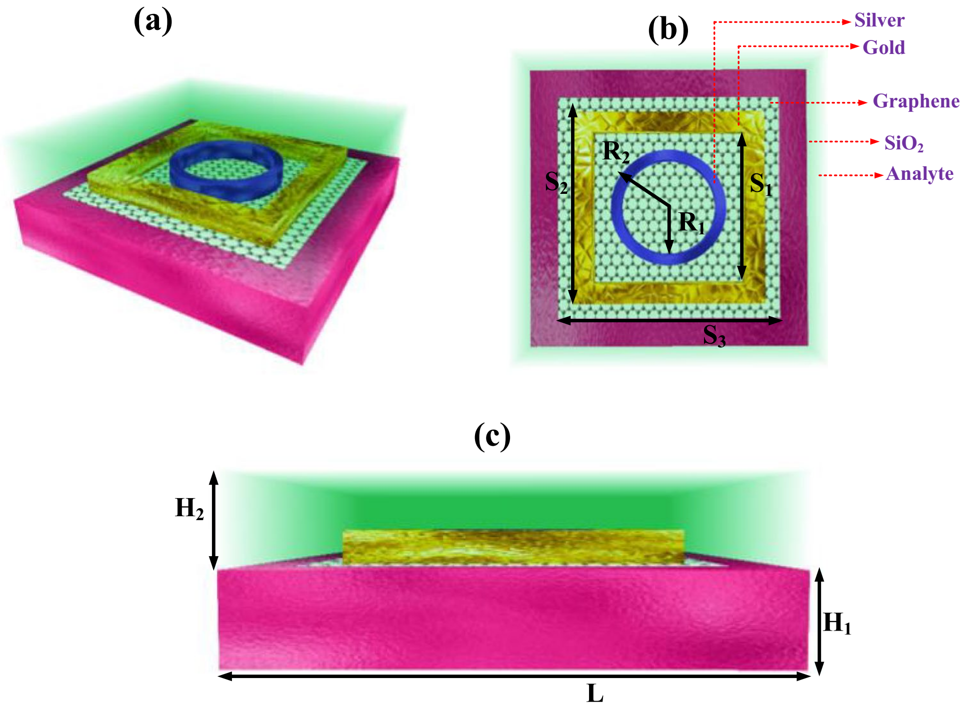

Fig. 1 The conceptual layout of the sensor from various perspectives: **a** in three dimensions, **b** top view, and **c** frontal view

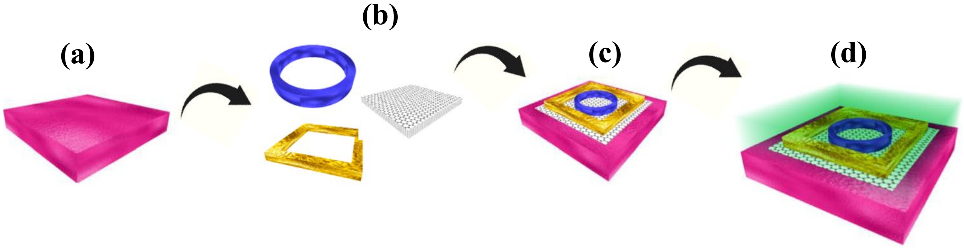

Fig. 2 The fabrication of the sensor proposed in this study. This fabrication sequence integrates photolithography, metal deposition, and dielectric layer deposition techniques

The graphene layer is then patterned to create square and circular ring resonators. This involves applying a photoresist layer, exposing it through a photomask to define the desired patterns, and developing the exposed photoresist to expose the graphene shape. A thin layer of silver (Ag) is deposited over the graphene to form the circular ring resonator structure. Subsequently, another layer of SiO_2 is deposited on top to provide insulation and spacing between the resonators and the layers above. The process is repeated for the square ring resonator: lithography is used to define its shape, followed by metal deposition to form the structure. After the final cleaning step to remove residues and contaminants, the fabricated sensor undergoes optional characterization tests to verify dimensions and ensure proper functionality.

Working of the Proposed Sensor Design

In real-time operation, the graphene-based metasurface sensor for hemoglobin detection functions through a series of well-coordinated steps. Initially, a biological sample, such as blood, is collected from the patient. This sample undergoes preparation, which may involve dilution or other processing to ensure compatibility with the sensor and to concentrate the hemoglobin. Once the sample is ready, the sensor is calibrated and initialized, ensuring that the SiO2 substrate, graphene layer, and resonators are clean and properly aligned. The sensor is then integrated with the detection system, which includes an infrared (IR) radiation source and an infrared detector, forming a complete detection setup. The prepared blood sample is applied to the sensor's surface, where hemoglobin molecules bind to the sensor's graphene and metal nanostructures. Infrared radiation from the external source is directed at the sensor, interacting with both the sample and the sensor's plasmonic materials, which include silver and graphene resonators. This interaction generates plasmonic resonance peaks, highly sensitive to the presence of hemoglobin due to changes in the local refractive index. The infrared detector captures these resonance peaks, and any shifts in these peaks indicate the presence and concentration of hemoglobin in the sample (Fig. 3).

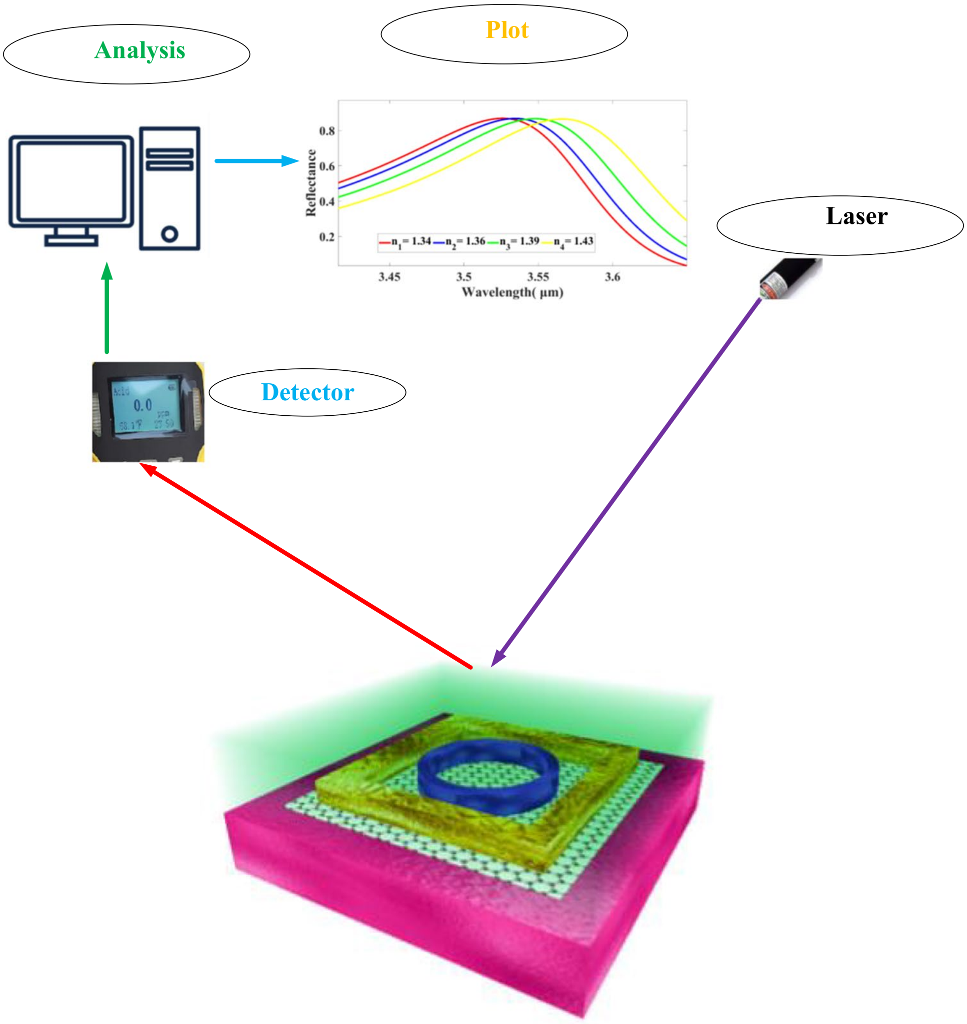

Fig. 3 The working principle of the sensor proposed in this study

Metasurface Analysis

Graphene's conductivity is a result of its unique electronic properties, including its zero band gap, high electron mobility, and its distinctive electronic behavior as massless Dirac fermions [27–31]. These characteristics make graphene a material of great interest for future electronic and nanotechnology applications. The conductivity of graphene and its relationship with the chemical potential are described by the following four equations [32]:

$$\varepsilon(\omega) = 1 + \frac{\sigma_s}{\varepsilon_0 \omega \nabla} \tag{1}$$

$$\sigma_{\text{intra}} = \frac{-je^2 k_B T}{\pi \hbar^2 (\omega - j2\Gamma)} \left(\frac{\mu_c}{k_B T} + 2ln\left(e^{\frac{\mu_c}{k_B T}} + 1 \right) \right) \tag{2}$$

$$\sigma_{\text{inetr}} = \frac{-je^2}{4\pi\hbar} \ln\left(\frac{2\left|\mu_c\right| - (\omega - j2\Gamma)\hbar}{2\left|\mu_c\right| + (\omega - j2\Gamma)\hbar} \right) \tag{3}$$

$$\sigma_s = \sigma_{\text{intra}} + \sigma_{\text{inter}} \tag{4}$$

The effectiveness of any sensor is evaluated using several performance metrics that highlight its sensitivity, resolution, and overall functionality. One key metric is sensitivity, which measures how the output frequency of the sensor changes in response to variations in the parameter being measured. Greater sensitivity means the sensor can detect smaller changes more effectively [33, 34]. The Figure of Merit assesses the sensor's efficiency by comparing its sensitivity to its full width at half maximum (FWHM). A higher Figure of Merit indicates superior performance, suggesting that the sensor has high sensitivity relative to

Table 1 Refractive indices of various hemoglobin compounds

RIs	n_1	n_2	n_3	n_4
Value (RIU)	3.4	3.6	3.9	4.3
Concentration	10	20	30	40

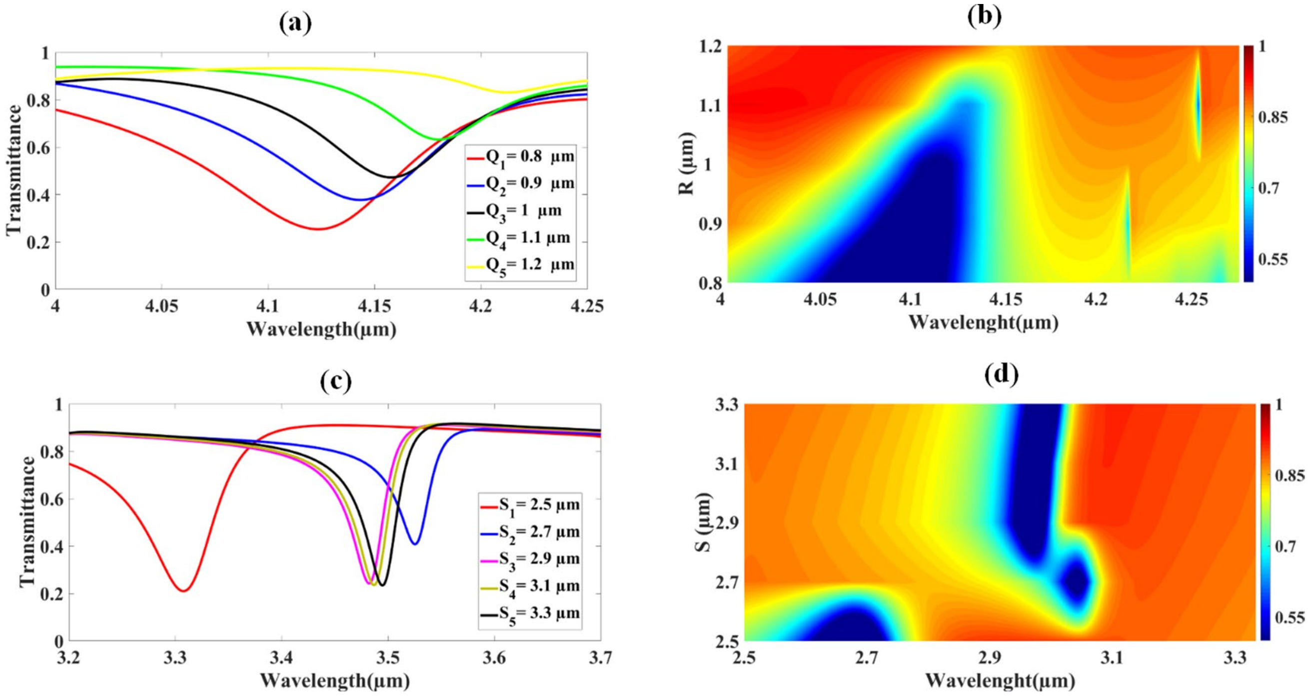

Fig. 4 The variations in transmittance response with respect to the alterations in the dimensions of the circular and the square resonators

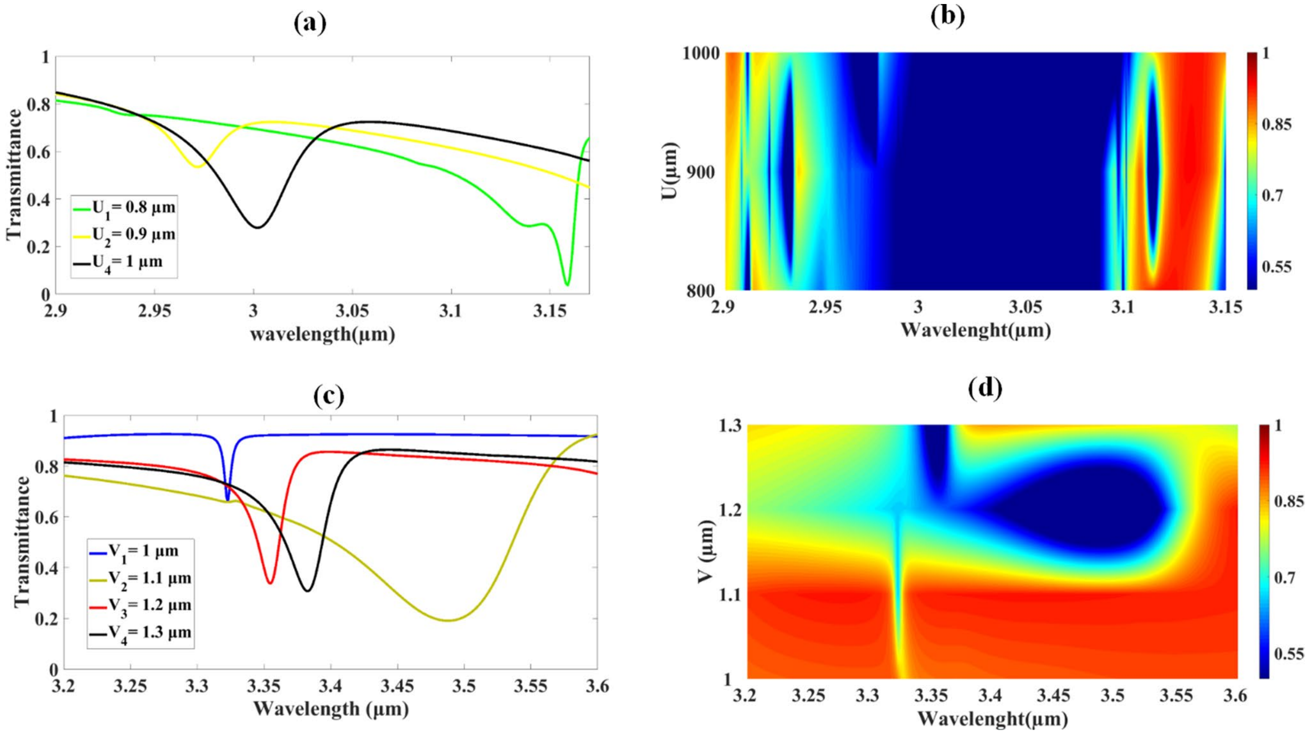

Fig. 5 The transmittance response as dimensions of circular and square ring resonators varied. The effect of decreasing the circular and increasing square resonator dimensions is also assessed

its resolution [35]. Another significant metric is the quality factor, which indicates the sharpness of the sensor's resonance. This factor compares the resonance frequency to the FWHM, with a higher value indicating a more accurate and narrowly resonant sensor [36]. The detection limit defines the smallest amount of the measured parameter that the sensor can reliably detect, considering its sensitivity, resolution, and overall performance. A lower detection limit signifies that the sensor is more precise at identifying small changes [37]. Dynamic range quantifies the sensor's capability to accurately handle varying signal levels. It is calculated as the ratio of the resonance frequency to the square root of the FWHM. A higher dynamic range suggests that the sensor can manage a wider range of signal intensities [38]. The signal-to-noise ratio measures the clarity of the signal against background noise. It is the ratio of the signal change to the noise level indicated by the FWHM. A higher signal-to-noise ratio reflects a clearer signal with less interference [39]. Sensor resolution integrates sensitivity with the detection limit to provide an overall assessment of the sensor's capacity to detect small changes in the measured parameter, taking into account both sensitivity and the minimum detectable quantity [40]. Lastly, the detector accuracy, which is the inverse of the FWHM, indicates the sensor's ability to differentiate between various signals. A larger detector accuracy suggests improved resolution in distinguishing closely spaced signals [41]. Equations 5–12 provide a summary of these parameters [42]:

$$S = \frac{\Delta f}{\Delta n} \tag{5}$$

$$\mathrm{FOM} = \frac{S}{\mathrm{FWHM}} \tag{6}$$

$$Q = \frac{fr}{\mathrm{FWHM}} \tag{7}$$

$$\mathrm{DL} = \left(\frac{\Delta n}{1.5}\right) \times \left(\frac{\mathrm{FWHM}}{\Delta f}\right)^{1.25} \tag{8}$$

$$\mathrm{DR} = \frac{f_r}{\sqrt{\mathrm{FWHM}}} \tag{9}$$

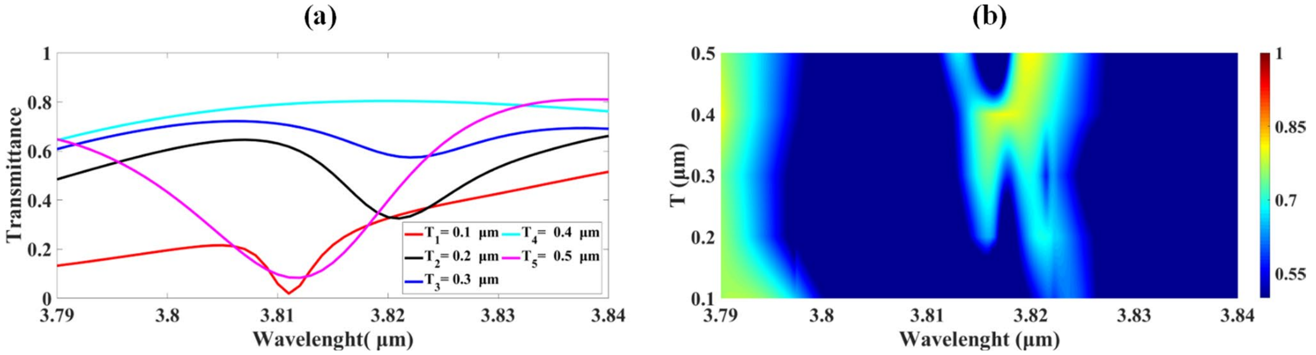

Fig. 6 The variation of transmittance response in the form of line and colour plots as the thickness of the metasurface resonators changes

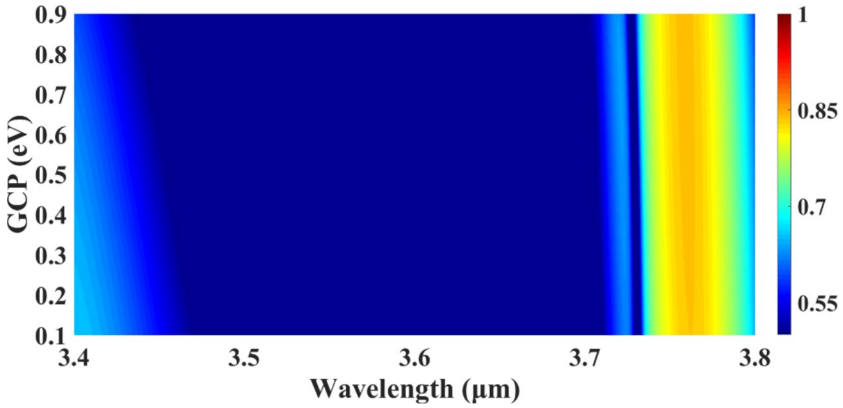

Fig. 7 The effect of GCP variation on transmittance drop in the form of the Fermi plot

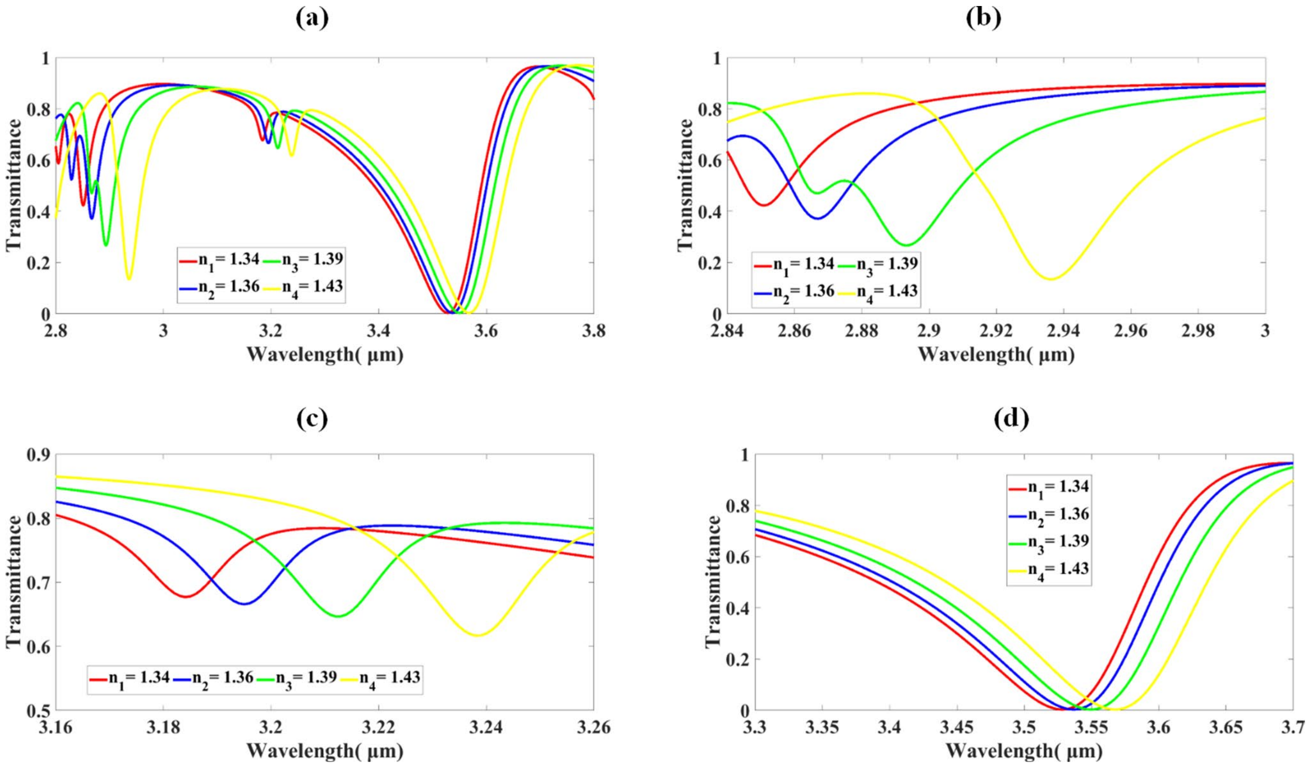

Fig. 8 The transmittance response varies with alterations in the refractive index of hemoglobin due to changes in concentration from 10 to 40 g/L

$$\mathrm{SNR} = \frac{\Delta f}{\mathrm{FWHM}} \tag{10}$$

$$\mathrm{SR} = S \times DL \tag{11}$$

$$\mathrm{DA} = \frac{1}{\mathrm{FWHM}} \tag{12}$$

SiO_2 refractive index is given by the Sellmeier equation [43].

$$n^2(\lambda) = 1 + \frac{B_1 C}{\lambda^2 - C_1} + \frac{B_2\lambda^2}{\lambda^2 - C_2} + \frac{B_3\lambda^2}{\lambda^2 - C_3} \tag{13}$$

The dielectric constant of gold is defined by [44].

$$\varepsilon_{Au} = \varepsilon_\infty - \frac{\omega_D^2}{\omega\left(\omega + j\gamma_D\right)} - \frac{\Delta_\varepsilon \Omega_L^2}{\left(\omega^2 - \Omega_L^2\right) + j\Gamma_L\omega} \tag{14}$$

The relationship between reflectance, angle of incidence, graphene potential, and conductivity is illustrated in the equations below [45].

$$r\left(\omega, \theta_i\right) = \frac{cos\theta_i \prod_{00}\left(\omega, \theta_i\right)}{2ick^2 + \omega cos\theta_i \prod_{00}\left(\omega, \theta_i\right)} \tag{15}$$

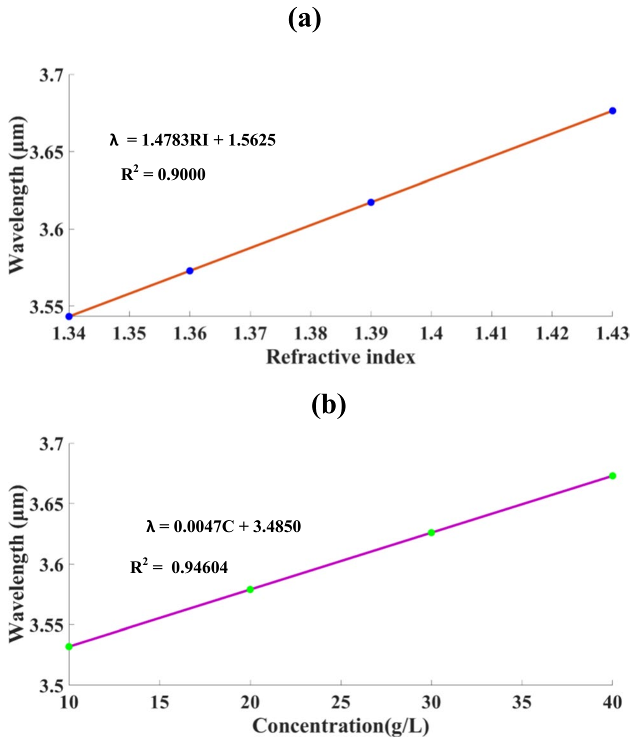

Fig. 9 The transmittance response varies due to changes in concentration from 10 to 40 g/L

$$\sigma_{||}(\omega,\mathrm{k}) = X = -i\frac{\omega}{4\pi\hbar k^2}\prod\nolimits_{00}(\omega,\mathrm{k}) \tag{16}$$

$$r(\omega,\theta_i) = \frac{2\pi cos\theta_i\sigma_{||}(\omega,\mathrm{k})}{c + 2\pi cos\theta_i\sigma_{||}(\omega,\mathrm{k})} \tag{17}$$

$$R(\omega,\theta_i) = |r(\omega,\theta_i)|^2 \tag{18}$$

$$R(\omega,\theta_i) = \frac{4\pi^2cos^2\theta_i[Re^2X + Im^2X]}{[c + 2\pi cos\theta_iReX]^2 + 4\pi^2cos^2\theta_iIm^2X} \tag{19}$$

$$R(\omega) = R(\omega,0) = \frac{4\pi^2[Re^2\sigma(\omega) + \mathrm{Im}^2\sigma(\omega)]}{[c + 2\pi Re\sigma(\omega)]^2 + 4\pi^2Im^2\sigma(\omega)} \tag{20}$$

The reflection coefficient, which measures how much light is reflected from the surface, is influenced by both the angular frequency of the light and the angle at which it strikes the surface. This coefficient is also affected by the graphene potential and the specific characteristics of the metasurface. Graphene's longitudinal conductivity is a crucial factor, representing its ability to conduct electricity. This conductivity is related to the angular frequency and wave vector of the incident light. The reflection coefficient can be expressed in terms of graphene's longitudinal conductivity. As the conductivity varies, so does the reflection coefficient, which in turn affects the overall reflectance of the biosensor. Reflectance is calculated by squaring the magnitude of the reflection coefficient. Consequently, any change in the reflection coefficient will be reflected in the final reflectance value. A more detailed expression for reflectance considers both the real and imaginary parts of the conductivity. This formula shows how the angle of incidence influences reflectance, highlighting the impact of changes in the real and imaginary components of conductivity. At normal incidence—when light strikes the surface perpendicularly—reflectance is calculated using the real and imaginary parts of the graphene conductivity. This case provides insights into the biosensor's performance under direct light incidence.

Table 2 The performance metrics for the proposed sensor

λ (μm)	3.52	3.59	3.64	3.66
n (RIU)	1.34	1.36	1.39	1.43
dλ (μm)		0.07	0.05	0.02
dn (RIU)		0.02	0.03	0.04
S (nm/RIU)		3500	1667	500
FWHM (μm)	0.2	0.199	0.2	0.199
FOM (RIU^{-1})		17.5879	8.33333	2.51256
Q	17.6	18.0402	18.2	18.392
DL		0.04922	0.11314	0.47125
DR	7.87096	8.04763	8.13929	8.20455
SNR		0.35176	0.25	0.1005
SR		0.17227	0.18856	0.23562
DA	5	5	5	5
X		0.0202	0.01571	0.00789

Refractive Index-Based Sensing

The refractive index is an essential optical property that indicates how light propagates through various substances. In medical and biological fields, measuring the refractive index is valuable for non-invasive analyses, such as assessing hemoglobin levels in blood [40, 41]. The refractive index of a substance is defined as the ratio

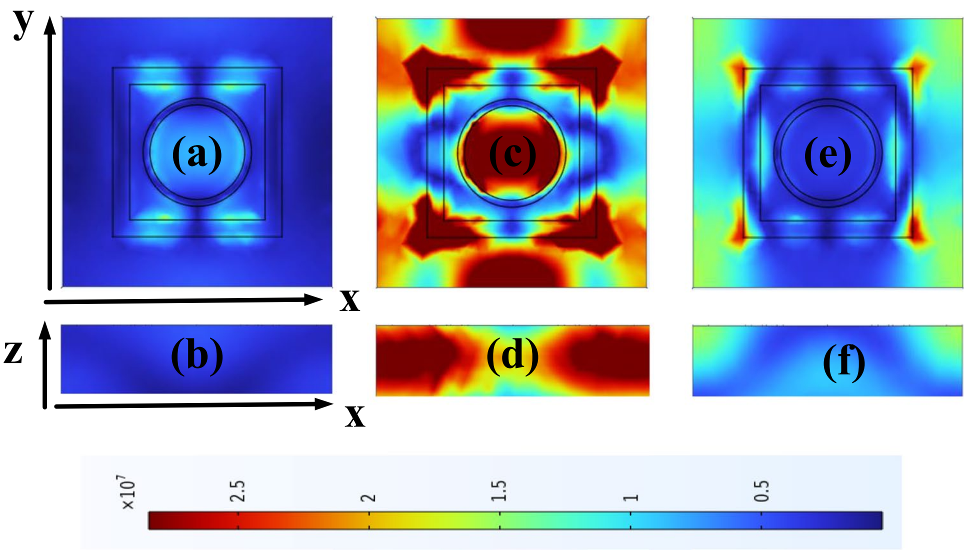

Fig. 10 The electric field distribution of the proposed design at three distinct wavelengths: (**a, b**) 3.3 μm, (**c, d**) 3.55 μm, and (**e, f**) 3.8 μm. The results indicate a significant enhancement in absorption, with the most pronounced effect observed at the 3.55 μm wavelength

Table 3 Comparison of the proposed sensor with other studies in the literature

	S	FOM (RIU^{-1})	D.L (RIU)	Materials	Application
Ref [50]	1600 nm/RIU	1107.18	0.0004	Cu	TB detection
Ref [51]	44.4 deg/100 fM	-	-	Graphene	Biodetection
Ref [52]	4000 nm/RIU^{-1}	17,416.66	-	-	Aqueous solution detection
Ref [53]	150GHzRIU^{-1}	0.039	-	Graphene	Detection of hemoglobin
Ref [54]	301.2°/RIU	-	-	Ti, Mxene, and $SrTiO_3$	Biosensing
Ref [55]	32,140°/RIU	-	-	$SrTiO_3$ and Ag	Biomedical applications
Proposed sensor	3500nmRIU^{-1}	17.6	0.05	Graphene, Au, and Ag	Detection of hemoglobin

of the speed of light in a vacuum to its speed in the substance. In biological tissues, this index varies based on the composition and concentration of different elements. Hemoglobin, a protein found in red blood cells, affects the refractive index of blood because of its distinctive optical properties. Hemoglobin's unique ability to absorb and scatter light differently from the surrounding blood plasma means that the concentration of hemoglobin impacts the blood's refractive index. Generally, a higher hemoglobin concentration results in a higher refractive index, allowing for hemoglobin levels to be inferred indirectly through changes in the refractive index [43, 46].

Various techniques employ the principle for hemoglobin detection. Optical methods, such as interferometry, measure changes in light interference patterns to detect variations in the refractive index [47]. Ellipsometry analyzes changes in light polarization after reflecting off a sample, revealing refractive index shifts due to hemoglobin. Optical coherence tomography (OCT) offers high-resolution tissue images by examining refractive index differences, which can be used to estimate hemoglobin

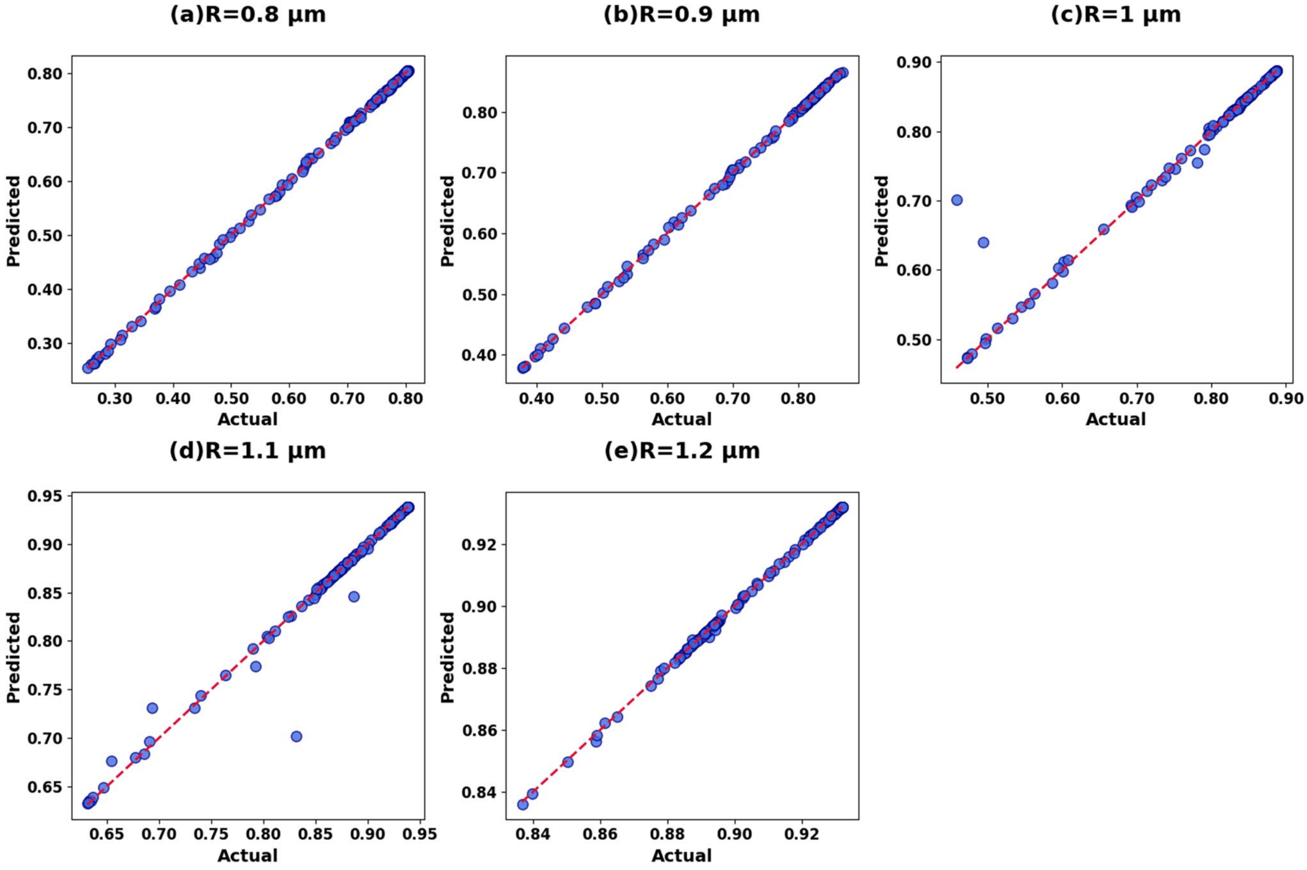

Fig. 11 The scatter plots(SP) for 1D-CNN regressor models trained using different R (dimensions of the circular ring resonator)

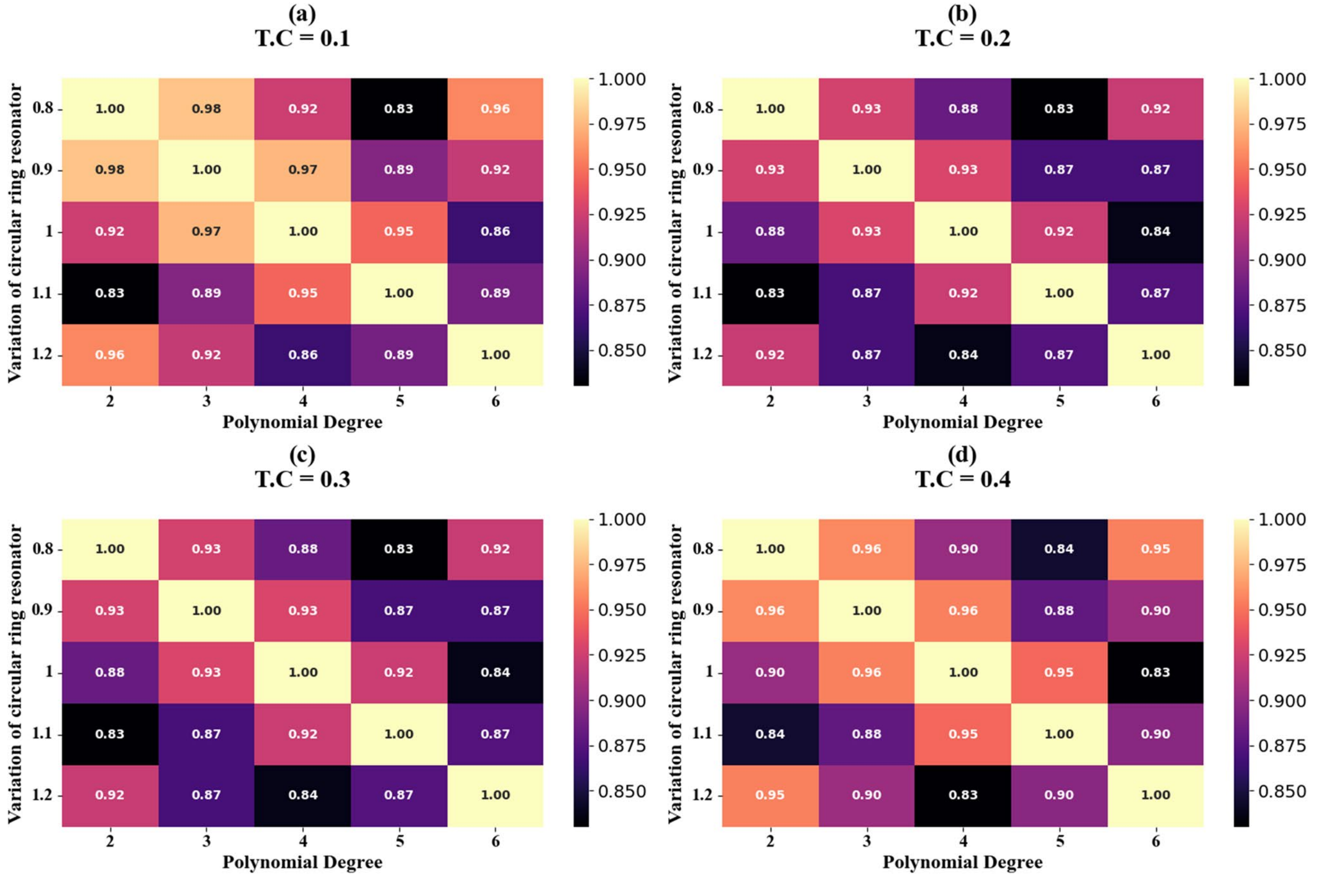

(a) T.C = 0.1	2	3	4	5	6
0.8	1.00	0.98	0.92	0.83	0.96
0.9	0.98	1.00	0.97	0.89	0.92
1	0.92	0.97	1.00	0.95	0.86
1.1	0.83	0.89	0.95	1.00	0.89
1.2	0.96	0.92	0.86	0.89	1.00

(b) T.C = 0.2	2	3	4	5	6
0.8	1.00	0.93	0.88	0.83	0.92
0.9	0.93	1.00	0.93	0.87	0.87
1	0.88	0.93	1.00	0.92	0.84
1.1	0.83	0.87	0.92	1.00	0.87
1.2	0.92	0.87	0.84	0.87	1.00

(c) T.C = 0.3	2	3	4	5	6
0.8	1.00	0.93	0.88	0.83	0.92
0.9	0.93	1.00	0.93	0.87	0.87
1	0.88	0.93	1.00	0.92	0.84
1.1	0.83	0.87	0.92	1.00	0.87
1.2	0.92	0.87	0.84	0.87	1.00

(d) T.C = 0.4	2	3	4	5	6
0.8	1.00	0.96	0.90	0.84	0.95
0.9	0.96	1.00	0.96	0.88	0.90
1	0.90	0.96	1.00	0.95	0.83
1.1	0.84	0.88	0.95	1.00	0.90
1.2	0.95	0.90	0.83	0.90	1.00

Fig. 12 The heat map table (HT) for 1D-CNN regressor models trained using different combinations of R

levels[48]. Spectroscopic techniques also contribute. Absorption spectroscopy assesses how hemoglobin absorbs light at specific wavelengths, providing concentration data. Raman spectroscopy detects molecular vibrations related to hemoglobin, allowing concentration determination from spectral changes. These refractive index-based techniques have practical uses in medical diagnostics. They can enable rapid, non-invasive anemia screening by detecting low hemoglobin levels and monitoring blood disorders like sickle cell disease or thalassemia. Additionally, advanced methods that combine refractive index measurements with other optical techniques could potentially offer non-invasive glucose monitoring by analyzing hemoglobin concentration changes (Table 1).

Results and Discussion

In this study, COMSOL Multiphysics version 6.2 is used for modeling the proposed biosensor. The design integrates a metasurface and undergoes comprehensive analysis, including the optimization of geometric parameters to enhance sensitivity and other critical performance metrics. The assessment focuses on evaluating transmittance, reflectance, and the spatial distribution of electric fields within the sensor. Additionally, we use machine learning techniques to predict the sensor's performance.

Parametric Analysis

The performance of the proposed sensor is intrinsically linked to its geometric parameters. To thoroughly explore this relationship, we conducted an extensive analysis focusing on two primary resonator types: the circular ring resonator and the square ring resonator.

This study aimed to investigate how variations in these resonators influence both transmittance and reflectance. Furthermore, we examined the combined effects of simultaneous adjustments to these resonators on transmittance. Initially, the analysis concentrated on varying the circular ring resonator, with the results presented in Figs. 4a, b. This investigation covers a wavelength range of 4 to 4.25 μm, varying the resonator size from 0.8 to 1.2 μm. Figure 4a illustrates the variation in transmittance across different dimensions of the circular ring resonator. The data presented include resonator sizes of 0.8 μm, 0.9 μm,

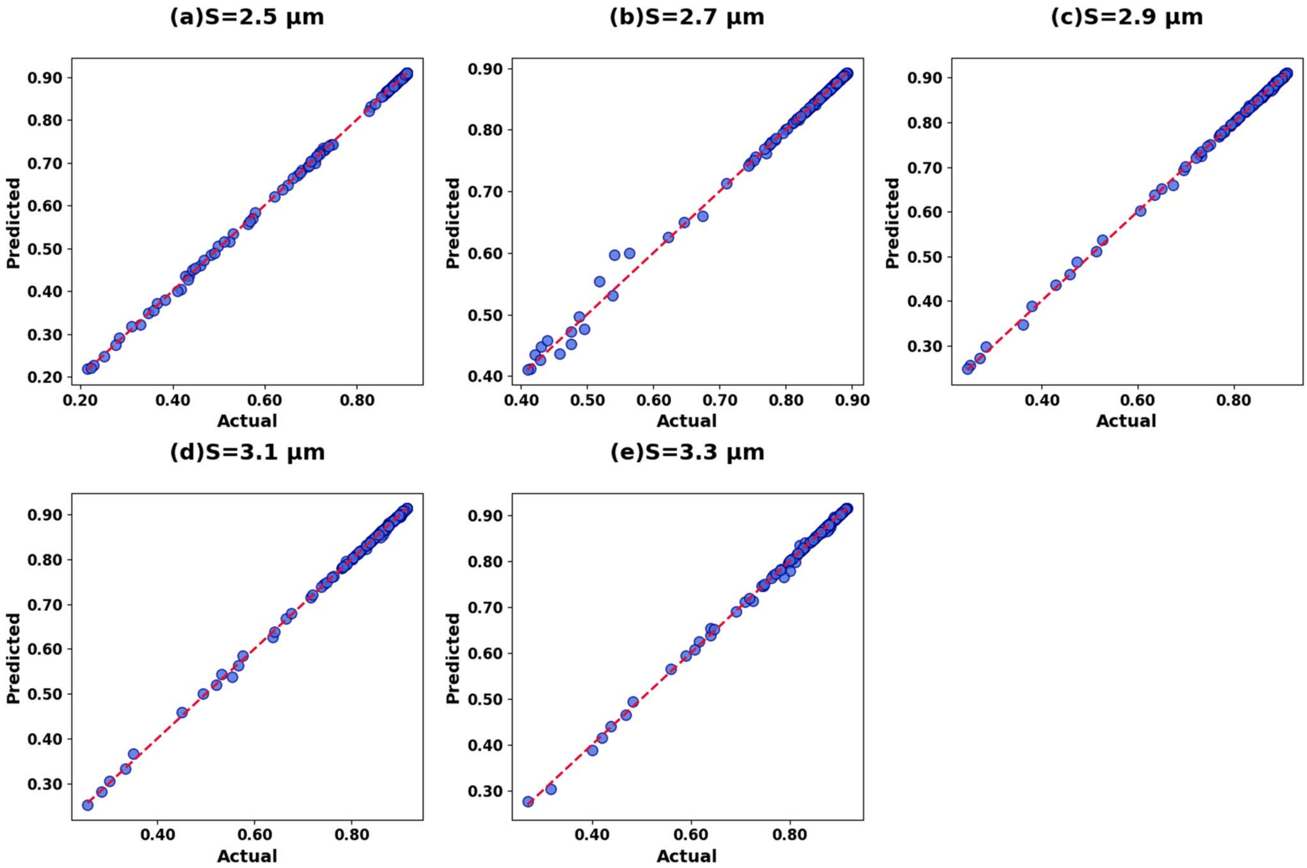

Fig. 13 The SP for 1D-CNN regressor models trained using different combinations of S (dimensions of square ring resonator)

1.0 µm, 1.1 µm, and 1.2 µm. A significant observation is the pronounced decrease in transmittance, which drops to 25.3% for a resonator size of 0.8 µm. Figure 4b demonstrates a clear correlation between the size of the ring resonator and the transmittance of the sensor. The data consistently show that larger resonator dimensions are associated with leftward shift in transmittance, a trend that is evident across the entire range of 4 to 4.25 µm wavelength band.

In the third case, a simultaneous adjustment of circular and square ring resonators was conducted. The first case involved the expansion of the circular ring while proportionally reducing the square ring. The results of this analysis are demonstrated in Figs. 5a, b. The dimensional range for both resonators was systematically varied from 0.8 µm to 1 µm. The analysis indicates a maximum transmittance drop of 11% when the diameter of the circular ring resonator is set at 0.8 µm. Figure 5b provides a fermi plot representation of the same results. In the fourth investigation, the study centered on evaluating the effect of decreasing the size of the circular ring while increasing the size of the square ring. The results are exemplified in Figs. 5c, d. Here, the dimensions of both resonators varied within the range of 1 µm to 1.3 µm. The study demonstrates a peak transmittance drop of 19.1% for the dimension of 1.2 µm. Figure 5d visually represents these results with a color-coded plot, demonstrating the relationship between resonator dimensions and transmittance variations.

In the fifth analysis, we investigated the effect of varying the resonators' thickness from 0.1 to 0.5 µm on sensor performance. This study focused on the sensor's response across wavelengths ranging from 3.79 to 3.84 µm. The results are illustrated in Figs. 6a, b, which depict the impact of resonator thickness on sensor behavior. Figure 6a demonstrates that the maximum transmittance drop is attained with the smallest dimension of 0.1 µm. Figure 6b provides a color-coded representation indicating the same results. Lastly, we examined how the graphene chemical potential (GCP) affects the transmittance response of the sensor. To do this, we varied the GCP from 0.1 to 0.9 eV in increments of 0.1 eV and displayed the resulting response in Fig. 7, using a color plot.

The influence of varying the graphene chemical potential (GCP) on the sensor's transmittance is depicted in Fig. 7, which spans a wavelength range of 3.4 to 3.8 µm. Figure 7 demonstrates clearly that with increasing GCP values, the transmittance response is affected progressively.

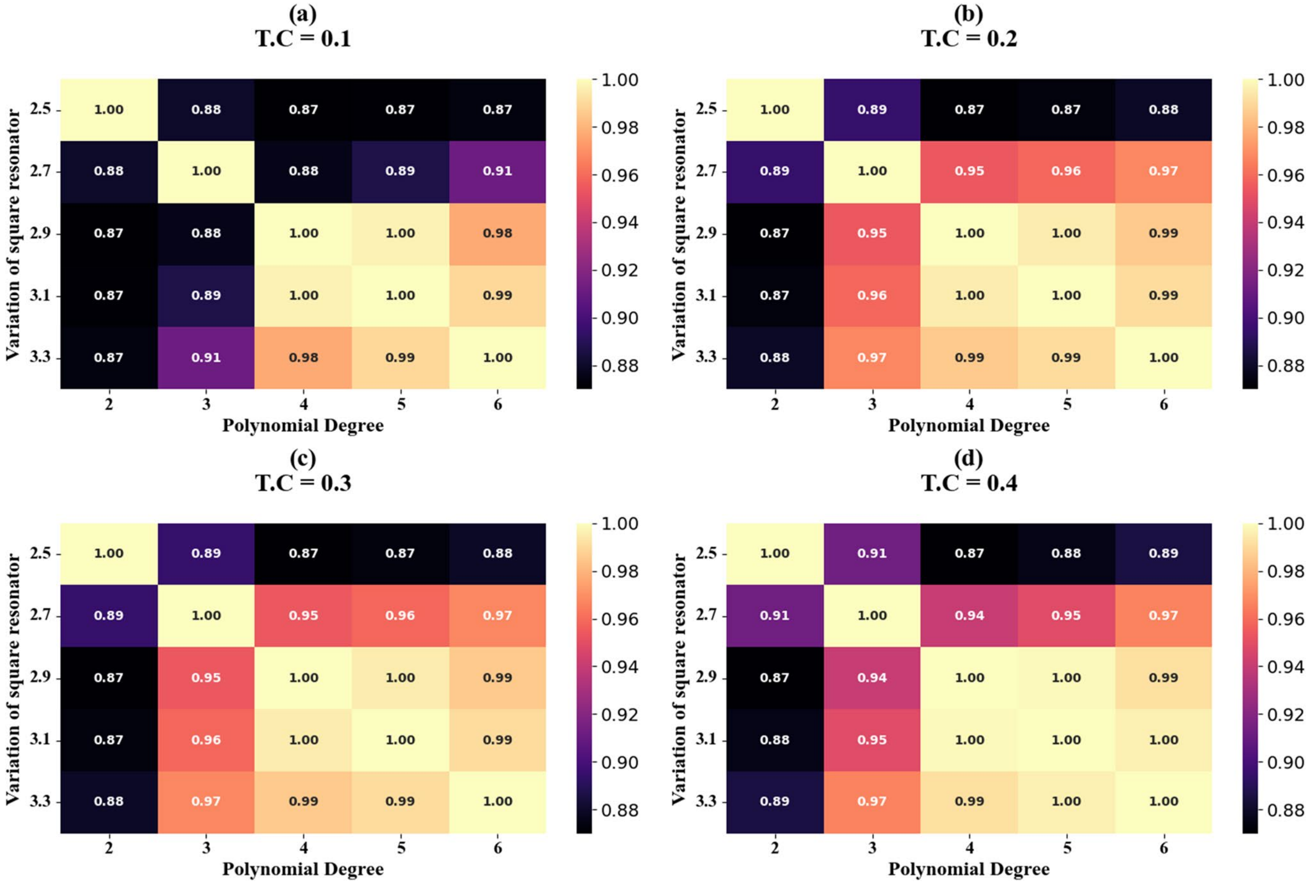

(a) T.C = 0.1	2	3	4	5	6
2.5	1.00	0.88	0.87	0.87	0.87
2.7	0.88	1.00	0.88	0.89	0.91
2.9	0.87	0.88	1.00	1.00	0.98
3.1	0.87	0.89	1.00	1.00	0.99
3.3	0.87	0.91	0.98	0.99	1.00

(b) T.C = 0.2	2	3	4	5	6
2.5	1.00	0.89	0.87	0.87	0.88
2.7	0.89	1.00	0.95	0.96	0.97
2.9	0.87	0.95	1.00	1.00	0.99
3.1	0.87	0.96	1.00	1.00	0.99
3.3	0.88	0.97	0.99	0.99	1.00

(c) T.C = 0.3	2	3	4	5	6
2.5	1.00	0.89	0.87	0.87	0.88
2.7	0.89	1.00	0.95	0.96	0.97
2.9	0.87	0.95	1.00	1.00	0.99
3.1	0.87	0.96	1.00	1.00	0.99
3.3	0.88	0.97	0.99	0.99	1.00

(d) T.C = 0.4	2	3	4	5	6
2.5	1.00	0.91	0.87	0.88	0.89
2.7	0.91	1.00	0.94	0.95	0.97
2.9	0.87	0.94	1.00	1.00	0.99
3.1	0.88	0.95	1.00	1.00	1.00
3.3	0.89	0.97	0.99	1.00	1.00

Fig. 14 The HT for 1D-CNN regressor models trained using different combinations of S

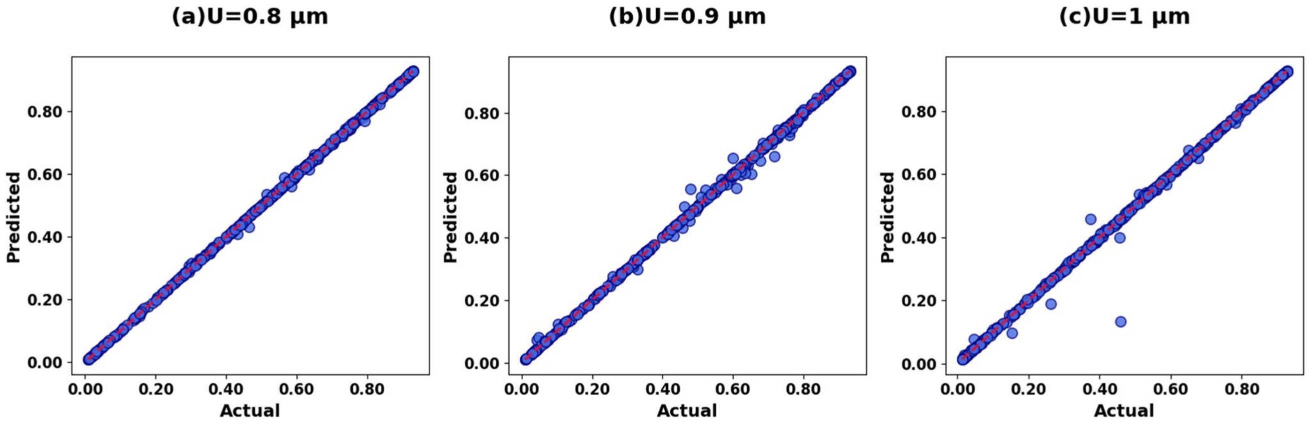

Fig. 15 The SP for 1D-CNN regressor models trained using different combinations of parameter U (variation of circular and square ring resonator)

Detection Analysis

After optimizing the design of the proposed metasurface-based sensor, we employed it to detect hemoglobin levels with heightened precision. Hemoglobin concentration fluctuations are known to affect the refractive index of the solution. In this study, the hemoglobin concentration varied across a specified range from 10 to 40 g/L, increasing in 10 g/L increments to cover a broad spectrum of concentrations. To ensure accuracy, we prepared solutions with hemoglobin concentrations of 10 g/L, 20 g/L, 30 g/L, and 40 g/L.Corresponding to these concentrations, we recorded

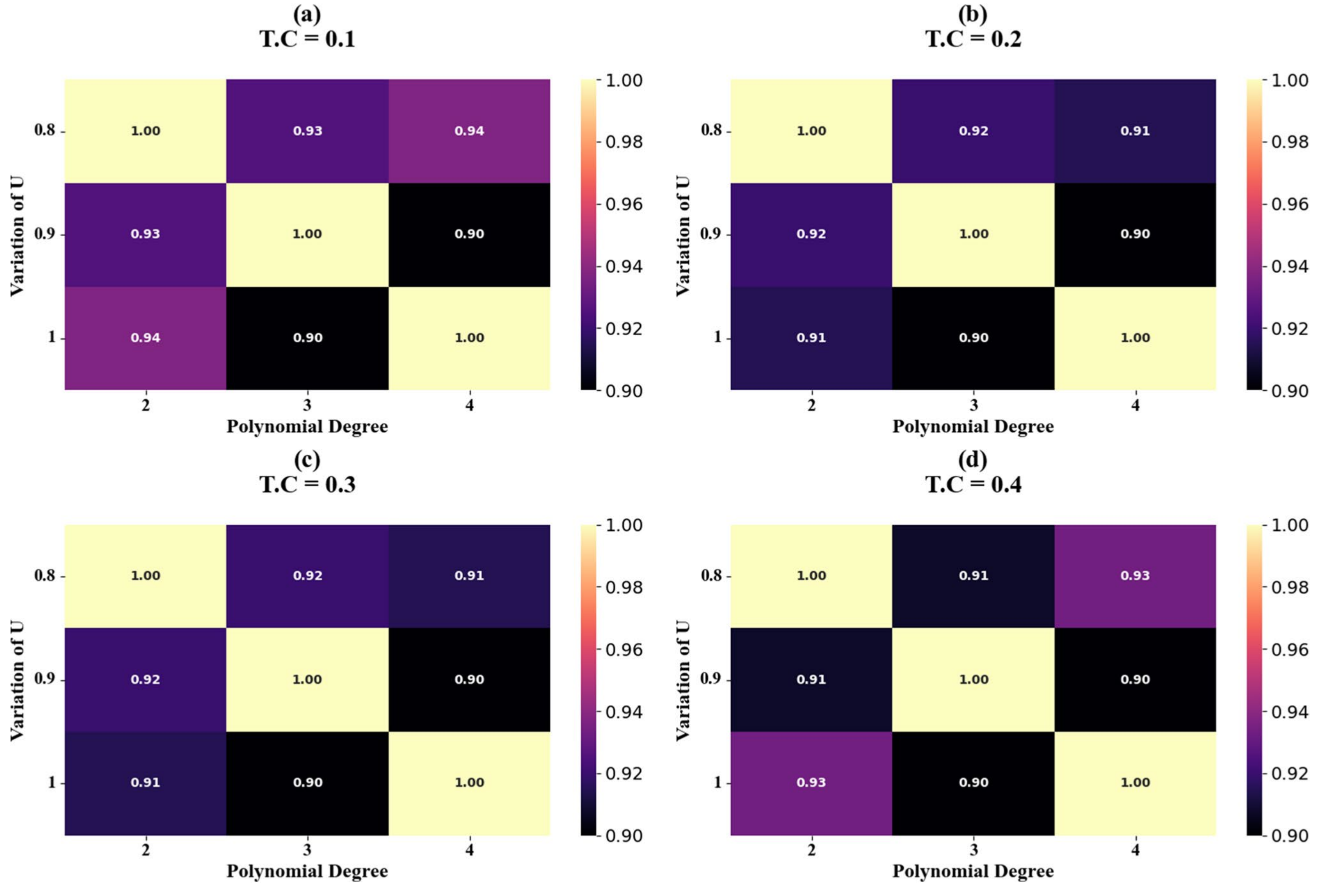

T.C = 0.1	2	3	4
0.8	1.00	0.93	0.94
0.9	0.93	1.00	0.90
1	0.94	0.90	1.00

T.C = 0.2	2	3	4
0.8	1.00	0.92	0.91
0.9	0.92	1.00	0.90
1	0.91	0.90	1.00

T.C = 0.3	2	3	4
0.8	1.00	0.92	0.91
0.9	0.92	1.00	0.90
1	0.91	0.90	1.00

T.C = 0.4	2	3	4
0.8	1.00	0.91	0.93
0.9	0.91	1.00	0.90
1	0.93	0.90	1.00

Fig. 16 The HT for 1D-CNN regressor models trained using different combinations of parameter U

the refractive indices as 1.34, 1.36, 1.39, and 1.43, respectively [49].

Figures 8a–d present the transmittance spectra for the proposed sensor design, demonstrating its performance in detection analysis. Figures 8a–d collectively depict the variation in transmittance as the refractive index increases from 1.34 to 1.43 across different wavelength ranges. Figure 8a illustrates a rightward in the transmittance response as the refractive index rises, indicating a shift towards longer wavelengths. This rightward shift signifies a modification in the sensor's optical behavior induced by the variation in the concentration of hemoglobin. The same results are depicted across 3.16–3.26 µm as exemplified in Fig. 8c as well as across the 3.3–3.7 µm wavelength band as depicted in Fig. 8d. The observed changes in transmittance are critical for assessing the sensor's sensitivity to refractive index variations. Moreover, we also conducted an extensive analysis to thoroughly inspect the relationship between various refractive indices (RIs) and the resonance wavelength (λ). The results of this in-depth investigation are depicted in the detailed Fig. 9a. Additionally, we also evaluated how different concentrations of hemoglobin relate to and impact the resonance wavelength, particularly focusing on evaluating where the distinct transmittance dips occur, as this information is crucial for effective detection. The outcomes and findings of this specific focused aspect of the broader study are presented in the informative Fig. 9b. Based on these comprehensive analyses, Eqs. 28 and 29 are attained.

$$\lambda = 1.4783RI + 1.5625 \tag{21}$$

$$\lambda = 0.0047C + 3.4850 \tag{22}$$

These empirically derived equations show a high degree of correlation, with impressive R^2 scores of 90% and 94.6% respectively.

Electric Field Analysis

Figure 10 illustrates the electric field distributions for the proposed sensor design at three wavelengths: 3.3 µm, 3.55 µm, and 3.8 µm. At a wavelength of 3.55 µm, there is a significant increase in absorption, as evidenced by the high electric field concentrations observed in Fig. 10c, d. These plots indicate a higher absorption of electromagnetic

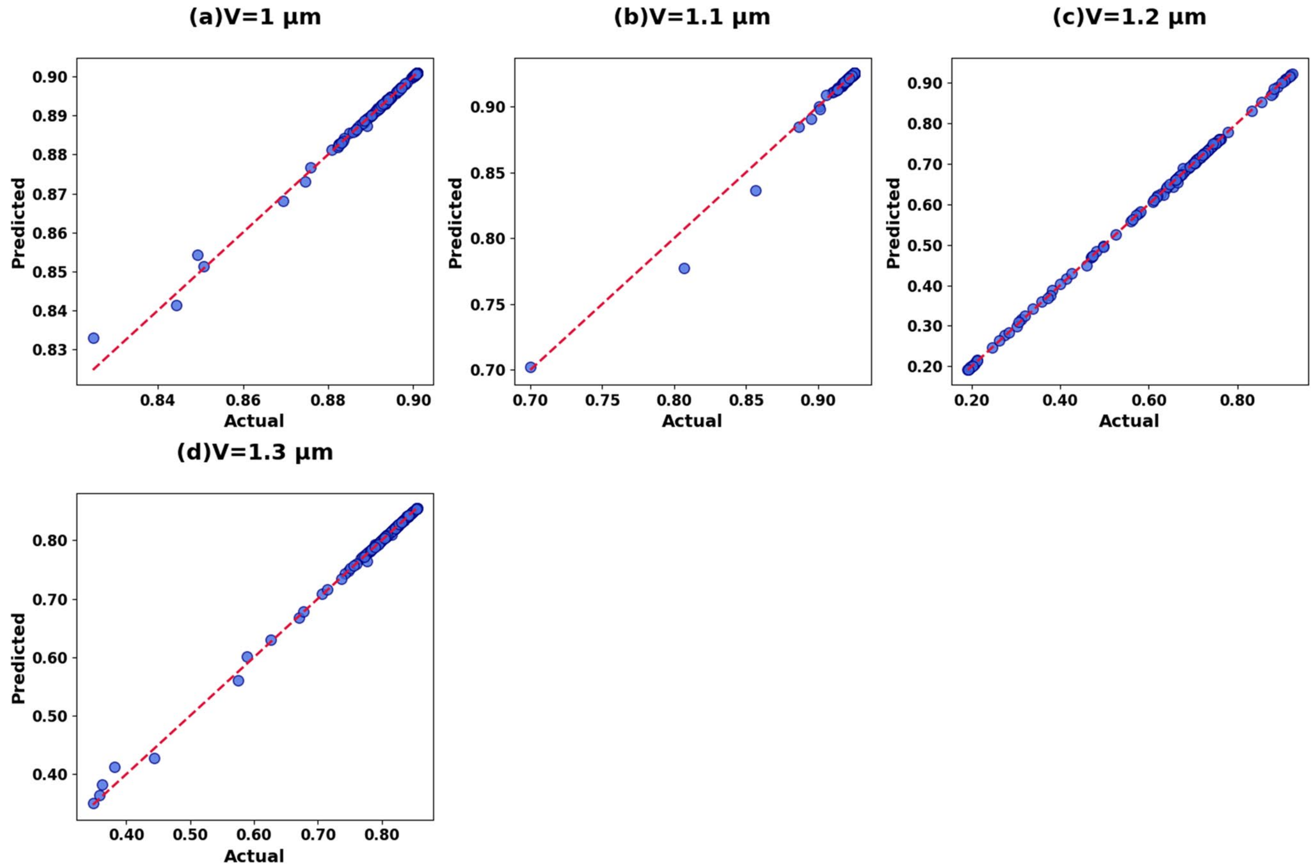

Fig. 17 The SP for 1D-CNN regressor models trained using different combinations of parameter V (variation of square and circular ring resonator)

energy at this wavelength. Conversely, at 3.3 µm and 3.8 µm, as depicted in Figs. 10a, b, e, and f, the electric field concentrations are markedly lower. This suggests that the sensor structure is optimized to enhance transmittance at these wavelengths, thereby reducing the absorption of incoming radiation. These observations highlight the variation in the sensor's absorption and transmission characteristics across different wavelengths, which is essential detection of the corresponding analytes.

Table 2 presents the performance parameters of the proposed sensor design. The table presents these parameters across different wavelengths (λ) ranging from 3.52 to 3.66 µm. The corresponding refractive indices (*n*) of blood components measured in refractive index units (RIU) are 1.34, 1.36, 1.39, and 1.43, respectively. The wavelength resolution (dλ) varies from 0.07 to 0.02 µm across these wavelengths. The sensor demonstrates sensitivities (S) ranging from the minimal value of 500 nm/RIU to the optimal value of 3500 nm/RIU, indicating how much the wavelength shifts per unit change in refractive index. The minimal full width at half maximum is 199 GHz. The quality factor (*Q*) values range from 17.6 to 18.392. The detection limits (DL) vary between 0.04922 RIU and 0.47125 RIU, while the dynamic range (DR) values span from 7.87096 to 8.20455. The sensor resolution (SR) values show minor fluctuations between 0.17227 and 0.23562, highlighting the sensor's ability to resolve fine changes. The maximum detection accuracy is 5. Lastly, the uncertainties (*X*) range from 0.0202 to 0.00789. Moreover, a comparative analysis was performed between the proposed designs and those previously published, with the results presented in Table 3. The findings clearly show the exceptional performance of the proposed sensor design.

Machine Learning Optimization Using 1D-CNN Regression Model

Convolutional neural networks (CNNs) have transformed computer vision and image processing tasks. Although they are widely recognized for their effectiveness with two-dimensional (2D) data, they have increasingly been applied to one-dimensional (1D) data. This trend is particularly notable in tasks involving sequential or time-series data,

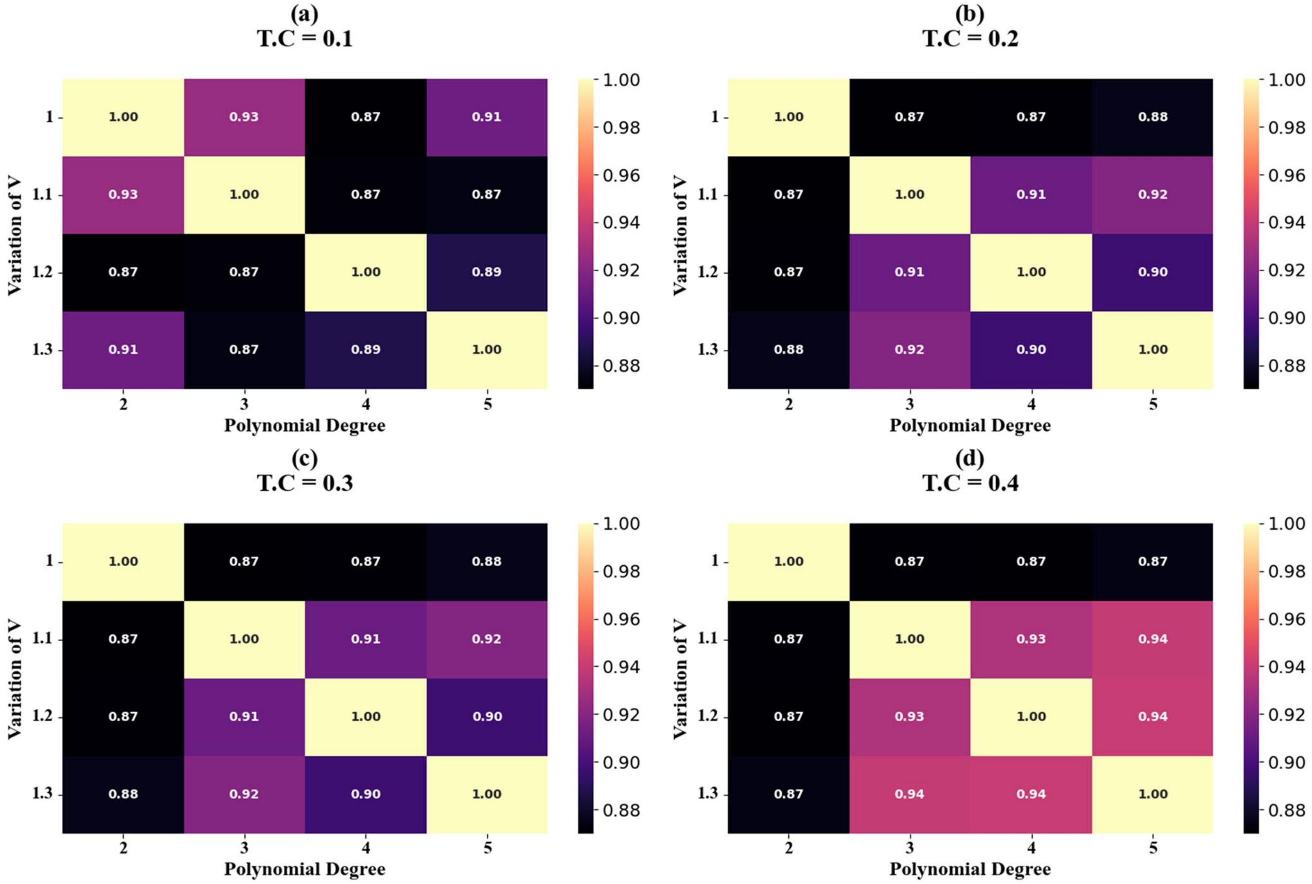

Fig. 18 The HT for 1D-CNN regressor models trained using different combinations of parameter V

where 1D-CNN regression models are utilized for prediction purposes [56]. The 1D-CNN regression model is an adaptation of the classic CNN design specifically designed for processing one-dimensional data, like sensor readings, audio signals, or time-series data from diverse domains. These models harness CNNs' convolutional operations and hierarchical feature extraction abilities to glean significant representations from the input data. This enables them to discern complex patterns and dependencies effectively [57]. A typical architecture of a 1D-CNN regression model includes several convolutional layers, where each layer employs one-dimensional filters that slide across the input sequence. These filters extract local features by applying learnable weights to segments of the input data. Following the convolutional layers, pooling layers are often used to downsample the feature maps. This downsampling helps in achieving translation invariance, thereby enhancing the model's ability to handle minor variations in the input data [58]. Once the convolutional and pooling stages in a 1D-CNN regression model have processed the input sequence and extracted relevant features, the resulting feature maps are flattened into a one-dimensional vector. This flattened representation is then fed into one or more fully connected layers (also known as dense layers). These fully connected layers integrate the learned features across the entire sequence and prepare them for prediction. In the context of regression tasks, the final output layer usually consists of a single neuron. This neuron outputs a continuous numerical value, which represents the predicted target variable based on the learned features from the preceding layers. This output is directly interpretable as the model's prediction for the given input sequence[59]. Using 1D-CNN regression models offers several advantages. One significant benefit is their capacity to autonomously extract pertinent features from input data, eliminating the necessity for extensive manual feature engineering. Moreover, these models excel at capturing prolonged dependencies and temporal patterns within data, rendering them highly suitable for tasks like time-series forecasting and anomaly detection, as well as various regression-based prediction tasks. Additionally, 1D-CNN regression models lend themselves well to augmentation or integration with other neural network architectures. For instance, they can be seamlessly combined with recurrent neural networks (RNNs) or attention mechanisms [60]. This integration enhances their modeling capabilities, allowing them to better adapt to diverse

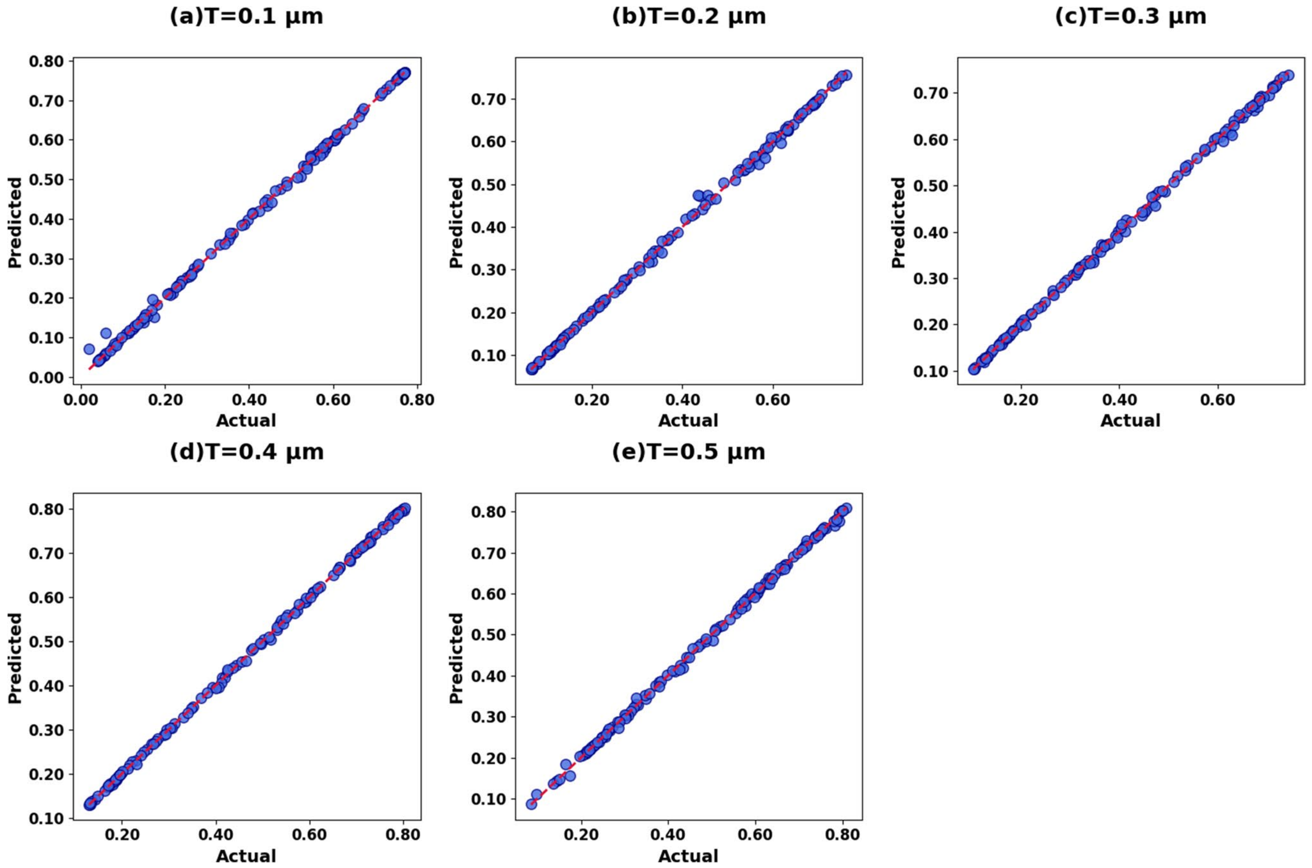

Fig. 19 The SP for 1D-CNN regressor models trained using different combinations of parameter T (resonator thickness)

problem domains and unique data characteristics. Thus, 1D-CNN regression models stand out for their versatility and effectiveness in tackling a broad spectrum of predictive tasks [61].

The study aims to rigorously assess the predictive accuracy of a regression model by subjecting it to various test cases denoted. Each test case involves the random extraction of subsets from the dataset. The remaining data is used for training the model to ensure robustness and generalizability. The evaluation metric employed is the coefficient of determination (R^2 score), which measures how well the model can predict the variance in the target variable based on the input features. This metric is essential for quantifying the model's predictive performance and its ability to capture the underlying relationships in the data.

Some of the equations employed in the model analysis include the following:

Convolution operation [62]

$$(f \times g)(t) = \int f(\tau)g(t-\tau)d\tau \tag{23}$$

ReLU activation function [63]

$$(\mathrm{f} \times \mathrm{g})(\mathrm{t}) \tag{24}$$

Batch normalization [64]

$$\mathrm{y} = \frac{\gamma \times ((\mathrm{x} - \mu)}{\sqrt{(\sigma^2 + \varepsilon) + \beta}} \tag{25}$$

Dropout [65]:

$$y = f(x) \times mask, where mask \sim Bernoulli(p) \tag{26}$$

Loss function (e.g., mean squared error) [66]:

$$\mathrm{MSE} = \left(\frac{1}{N}\right)\mathrm{x} \sum (\mathrm{i} = 1 \text{ to } \mathrm{N})(\mathrm{y_i} - \hat{\mathrm{y}}_\mathrm{n}^2) \tag{27}$$

Gradient descent update rule

$$\theta = \theta - \alpha \times \nabla J(\theta) \tag{28}$$

The coefficient of determination

$$\mathrm{R}^2 = \frac{\sum_{\mathrm{i}=1}^{\mathrm{N}} (\text{Predicted Target Value}_\mathrm{i} - \text{Actual Target Value}_\mathrm{i})}{\sum_{\mathrm{i}=1}^{\mathrm{N}} \left(\text{Actual Target}_\mathrm{i} - \text{Average Target Value}\right)^2} \tag{29}$$

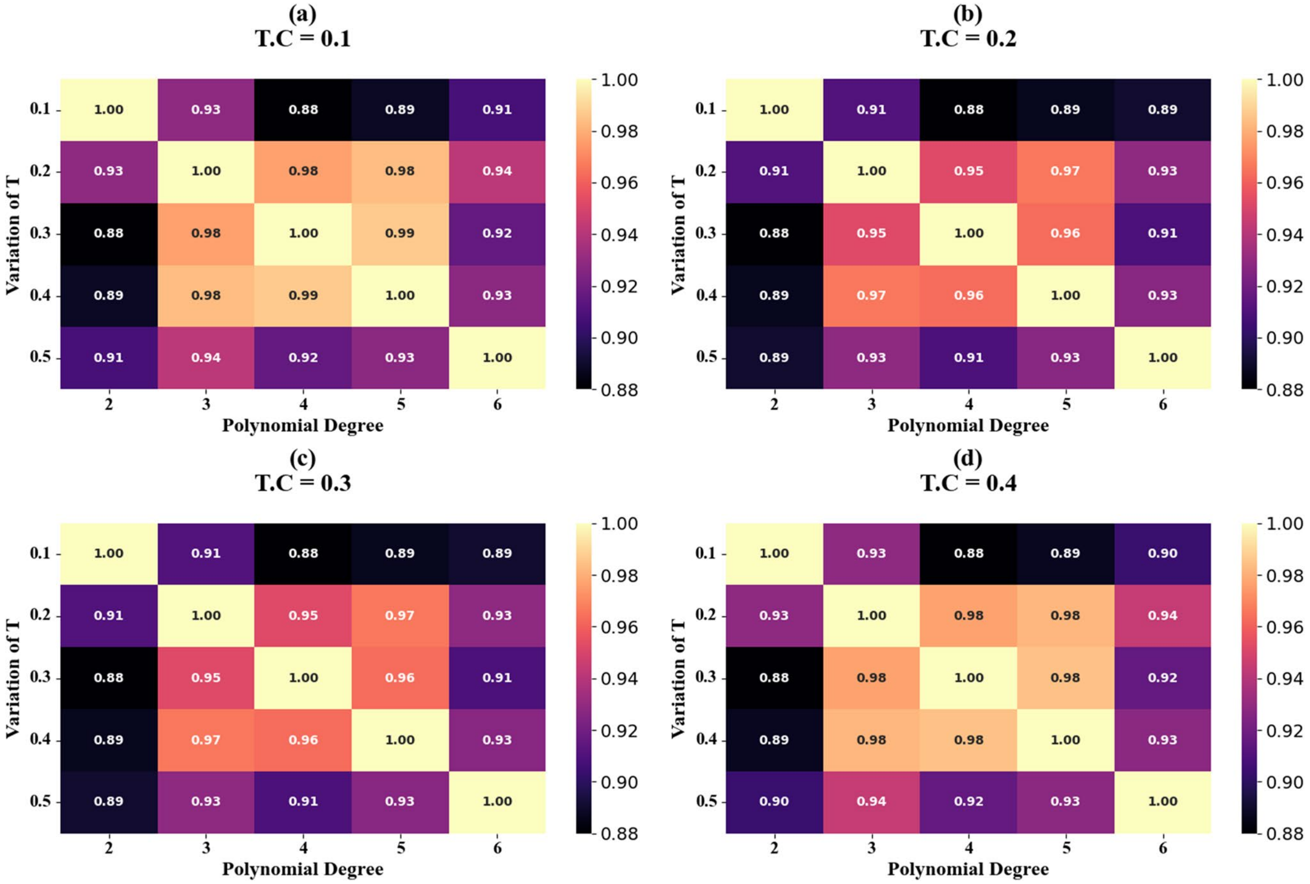

Fig. 20 The HT for 1D-CNN Regressor models trained using different combinations of parameter T

We have conducted a prediction analysis of the R^2 scores for variations in the circular ring resonator, with the results detailed in Figs. 11a–e and 12a–d for various test cases (TC). These figures present the prediction accuracy across different combinations of circular ring resonator dimensions and polynomial degree features, leveraging both SP and HT plots. As exemplified Figs. 11a–e demonstrate that the highest R^2 scores of 99.99% (TC = 0.2), 99.96% (TC = 0.25), 99.97% (TC = 0.3), 99.95% (TC = 0.35), and 100% (TC = 0.4) are achieved for resonator values of 0.8 µm, 0.9 µm, 1 µm, 1.1 µm, and 1.2 µm, respectively. Also, the heat map plots in Figs. 12a–d demonstrate an improvement in R^2 scores: from 0.96 to 1 for TC = 0.1, from 0.92 to 1 for TC = 0.2 and TC = 0.3, and from 0.95 to 1 for TC = 0.4. These enhancements result from an increase in the polynomial degree from 1 to 6.

The performance of 1D-CNN regression models trained various TC values is depicted in Figs. 13a–e and 14a–d. These figures show the model performance across different combinations of square ring resonator values and polynomial degree features, using both scatter plots (SP) and heat map (HT) visualizations. As demonstrated by the scatter plots, the R-squared (R^2) scores achieved by the models are 99.89% (TC = 0.1), 99.96% (TC = 0.2), 99.87% (TC = 0.26), 99.91% (TC = 0.3), and 99.99% (TC = 0.35) for resonator values of 2.5 µm, 2.7 µm, 2.9 µm, 3.1 µm, and 3.3 µm, respectively. These exceptionally high R^2 values indicate that the 1D-CNN models are able to explain over 99.8% of the variance in the target variable for these test cases. Again, the heat map plots in Figs. 12a–d demonstrate an improvement in R^2 scores as the polynomial degree is increased from 1 to 6. Specifically, the R^2 values increase from 0.87 to 1.0 for test case 0.1, from 0.88 to 1.0 for test cases 0.2 and 0.3, and from 0.89 to 1.0 for test case 0.4. These results suggest that higher-order polynomial features can significantly enhance the predictive performance of the 1D-CNN regression models for the given problem domain.

The R^2 scores for 1D-CNN regression models, evaluated across different test cases, are depicted in Figs. 15a–c and 16a–d. These figures illustrate the models' performance with various combinations of the U parameter and polynomial degree features, as shown in the SP and HT plots. Notably, the highest R^2 scores achieved are 99% for TC = 0.3, 99.9% for TC = 0.2, and 100% for TC = 0.35,

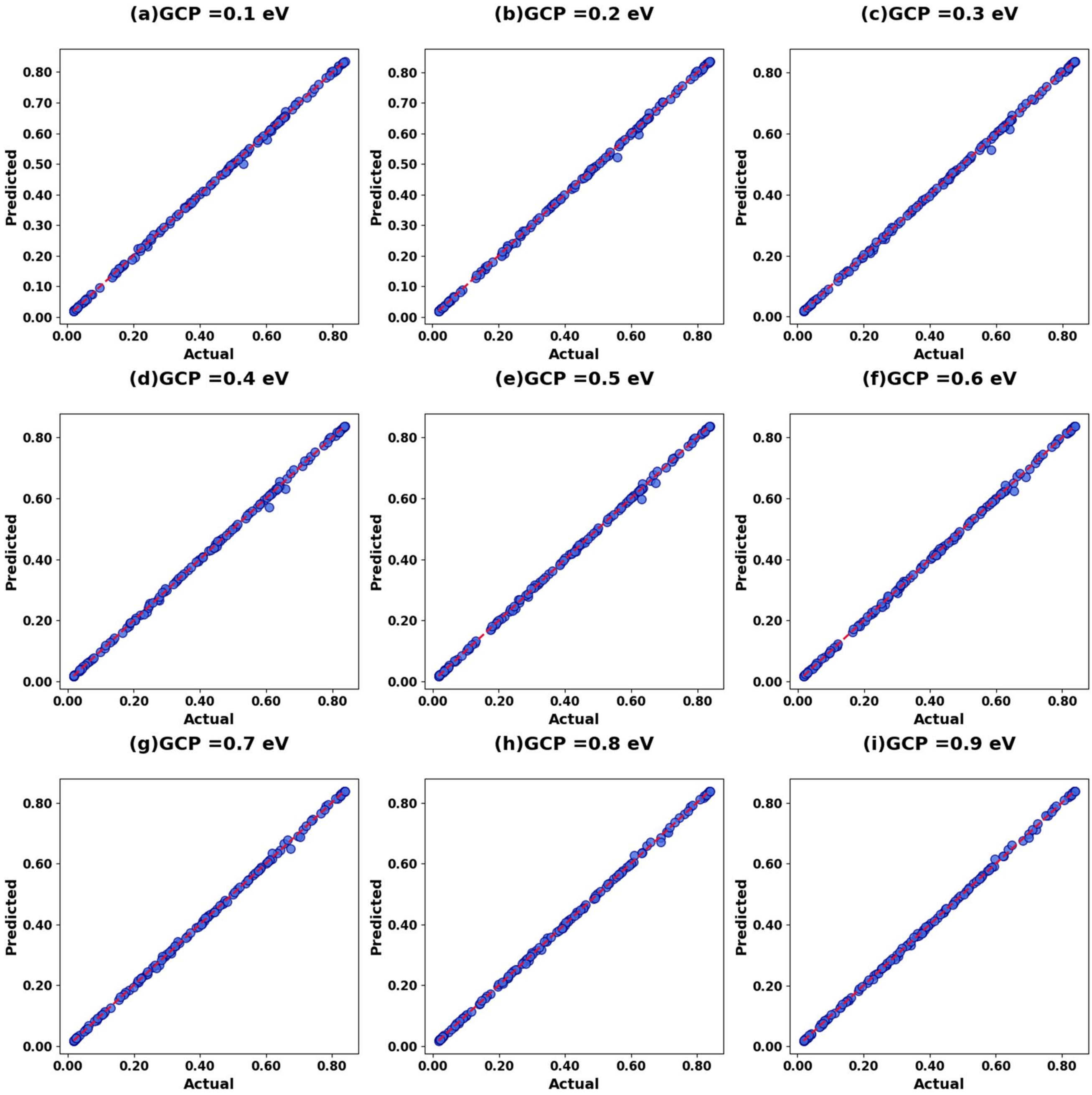

Fig. 21 The SP for 1D-CNN regressor models trained using different combinations of GCP values

corresponding to U values of 0.8 µm, 0.9 µm, and 1 µm, respectively. Moreover, the heat map plots in Figs. 16a–d reveal that increasing the polynomial degree from 1 to 6 leads to improved R^2 scores. Specifically, R^2 values range from 0.94 to 1.0 for test case 0.1, from 0.91 to 1.0 for test cases 0.2 and 0.3, and from 0.93 to 1.0 for test case 0.4. The same results are attained for the variation of parameters V and T as depicted by scatter plots in Figs. 17a–d, Fig. 18, and Fig. 19a–e and heat map plots in Figs. 18a–d and Figs. 20a–d, where an optimum R^2 score of 1 is attained.

The performance of the 1D-CNN regression models, trained on various TCs, is exemplified in Figs. 21a–i and 22a–d. These figures depict the models' behavior across different combinations of GCP values and polynomial degrees, represented by scatter plots (SP) and heat map (HT) visualizations. Notably, the models achieved exceptionally high R-squared (R^2) scores, ranging from 99.91

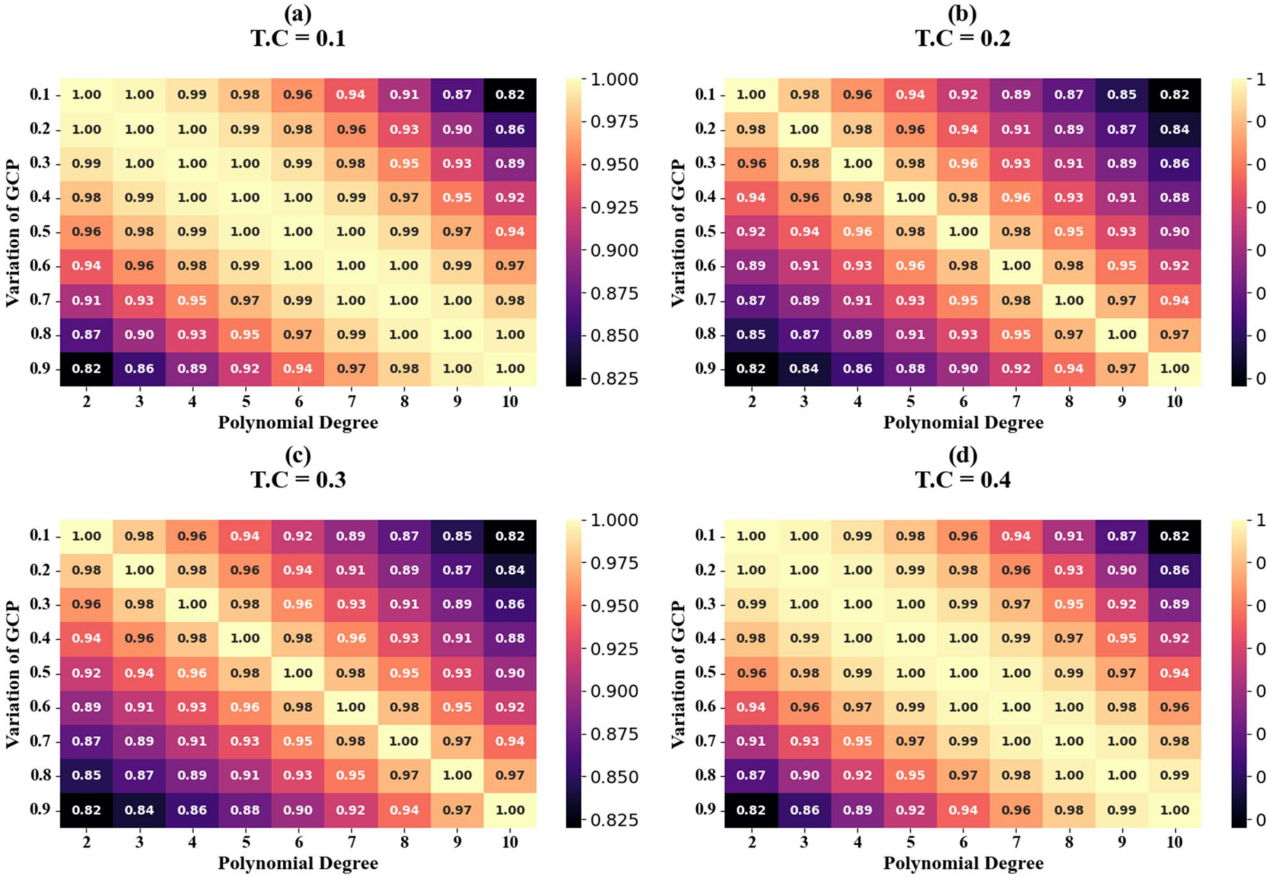

Fig. 22 The HT for 1D-CNN regressor models trained using different combinations of GCP values

to 99.99% for test case values of 0.26, 0.27, 0.28, 0.29, 0.30, 0.31, 0.32, 0.33, and 0.34. These results indicate that the 1D-CNN regression models are able to explain over 99.9% of the variance in the target variable for these test cases, demonstrating their strong predictive capability. Moreover, the heat map plots in Figs. 22a–d demonstrate that increasing the polynomial degree from 1 to 6 leads to improved R^2 scores. Specifically, the R^2 values range from 0.82 to 1.0 for test cases 0.1, 0.2, 0.3, and 0.4, indicating that higher-order polynomial features can significantly enhance the performance of the 1D-CNN regression models.

The effectiveness of the 1D-CNN regression models, which were trained on various test cases, is illustrated in Figs. 23a–d and 24a–d. The scatter plots in these figures show that the models achieved exceptional *R*-squared (R^2) scores of 99.94%, 99.95%, 99.96%, and 99.97% for test case (TC) values of 0.1, 0.15, 0.2, 0.25, and 0.3, respectively. These remarkably high R^2 values indicate that the 1D-CNN models are able to explain over 99.9% of the variance in the target variable for these test cases, demonstrating their strong predictive performance. On the other hand, the heat map plots in Figs. 24a–d demonstrate that increasing the polynomial degree from 1 to 6 leads to improved R^2 scores. Specifically, the R^2 values range from 0.93 to 1.0 for test cases 0.1, 0.2, 0.3, and 0.4.

Limitations and Future Work

While the proposed graphene-based metasurface sensor for hemoglobin detection shows promising results, it is important to acknowledge several limitations and potential avenues for future research. The current design focuses on a single sensor unit, and future work should explore scaling up the system to create sensor arrays or integrate multiple sensors on a single chip. This could enable simultaneous detection of multiple biomarkers or improve the spatial resolution of hemoglobin measurements. The sensor's performance under varying environmental conditions, such as temperature fluctuations and humidity, needs further investigation. Developing strategies to maintain accuracy and reliability in real-world settings is crucial for practical applications. Additionally, power efficiency

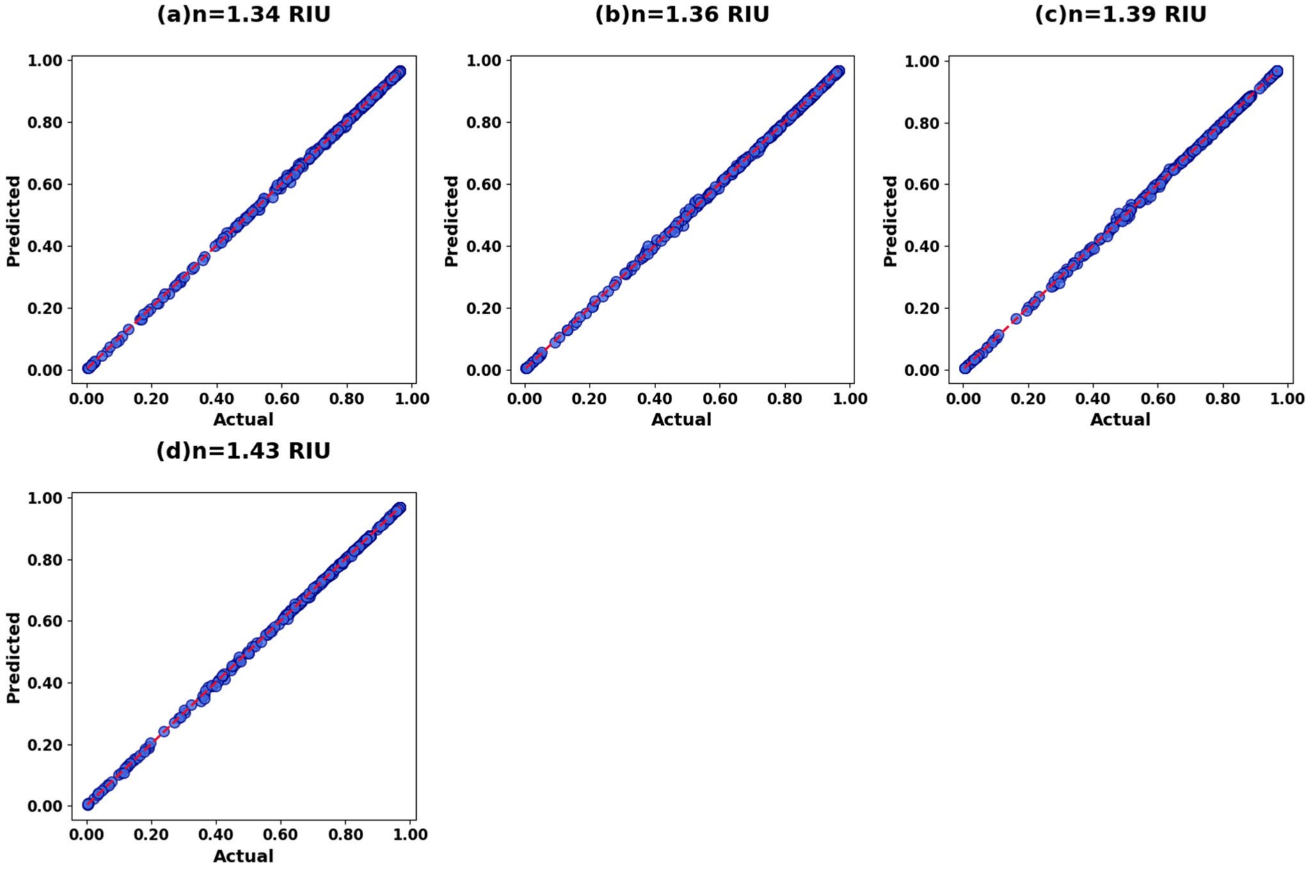

Fig. 23 The SP for 1D-CNN regressor models trained using different combinations of RI values

is an important consideration for portable or implantable devices. Future research should focus on optimizing the design for low power consumption without compromising sensitivity. While the sensor shows high sensitivity to hemoglobin, its selectivity in complex biological fluids containing multiple proteins and potential interferents should be thoroughly evaluated. Developing surface functionalization strategies to enhance specificity could be a valuable avenue for future work. The proposed design involves intricate nanostructures and multiple materials, so investigating cost-effective and scalable fabrication methods compatible with existing semiconductor manufacturing processes would be beneficial for commercialization. Adapting the sensor for continuous, real-time hemoglobin monitoring could greatly enhance its clinical utility. This may involve developing microfluidic systems for sample handling and exploring ways to improve the sensor's response time. While the current study demonstrates the potential of machine learning for predicting sensor behavior, future work could explore more advanced AI techniques for real-time data analysis, pattern recognition, and decision support in clinical settings. For in vivo applications, the biocompatibility and long-term stability of the sensor materials need to be thoroughly investigated. This includes studying the potential degradation of the graphene and metal nanostructures in biological environments. Further miniaturization of the sensor and associated readout electronics could enable the development of minimally invasive or implantable devices for continuous hemoglobin monitoring. Finally, extensive clinical studies comparing the sensor's performance to gold standard hemoglobin measurement techniques are necessary to validate its accuracy and reliability in diverse patient populations. Addressing these challenges and exploring these avenues for future research will be crucial for advancing the proposed hemoglobin sensor towards real-world

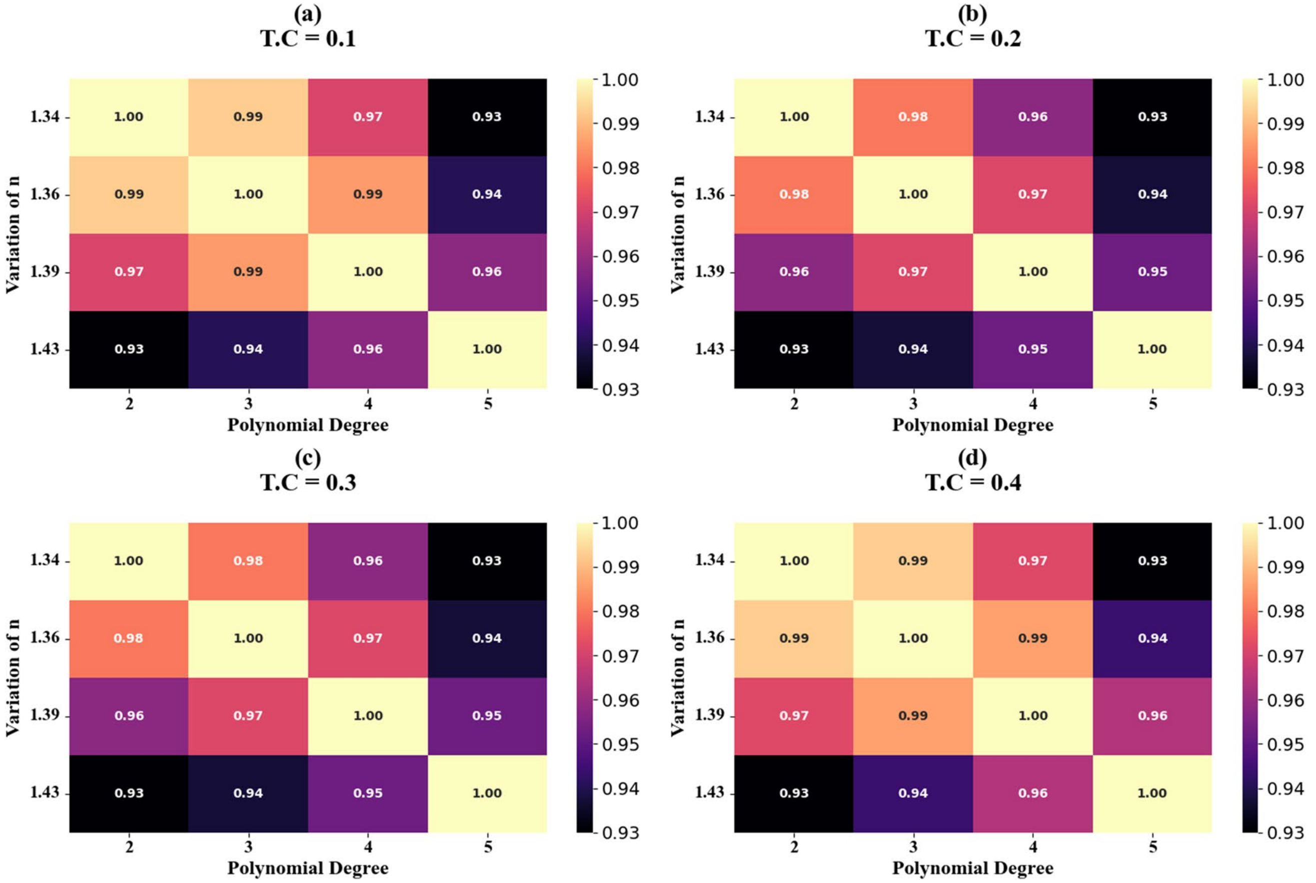

Fig. 24 The HT for 1D-CNN regressor models trained using different combinations of RI values

applications in healthcare and diagnostics. Collaborative efforts between materials scientists, biomedical engineers, and clinicians will be essential in overcoming these limitations and realizing the full potential of this technology.

Conclusion

To sum up, this study has presented an advanced approach to hemoglobin detection through the design and analysis of a graphene-based metasurface sensor. By integrating the exceptional optical and electronic properties of graphene with the plasmonic characteristics of silver and gold nanostructures, the proposed sensor exhibits enhanced sensitivity, resolution, and overall performance for the detection of hemoglobin. The comprehensive parametric analysis and optimization conducted in this work have demonstrated the sensor's ability to resolve changes in hemoglobin concentration through distinct shifts in transmittance and reflectance spectra. The resulting sensor design achieved a remarkable sensitivity of 3500 nm/RIU, a maximum figure of merit of 17.6, and a detection limit of 0.05 RIU, showcasing its superior performance compared to previously reported hemoglobin sensors. Furthermore, the integration of a 1D convolutional neural network regression model enhances the accuracy of the proposed sensor as well as reduces the time and resources required for simulation and optimization. The exceptional characteristics of the proposed graphene-based metasurface sensor, combined with its artificial intelligence-assisted performance prediction, establish it as a promising platform for various medical diagnostics and healthcare applications that require precise and sensitive hemoglobin monitoring. The sensor's ability to provide rapid, non-invasive, and reliable hemoglobin detection holds significant potential to improve patient care and facilitate timely diagnosis and monitoring of related health conditions.

Acknowledgements The authors would like to express their gratitude to the National Forensic Sciences University for granting access to the digital computer laboratory for this research, as well as to the ICCR for their scholarship support.

Author Contribution "Conceptualization, JW,NM; Methodology,JW,NM,OA; Software.JW,CL,OA; Validation, all authors; Writing—original draft preparation, All authors; Formal Analysis, JW,TT,CL; Writing—review and editing, All Authors; All authors have read and agreed to the published version of the manuscript."

Data Availability The data supporting the findings in this work are available from the corresponding author with a reasonable request.

Declarations

Ethical Approval Not applicable.

Competing Interests The authors declare no competing interests.

References

1. Quaye IK (2015) Extracellular hemoglobin: the case of a friend turned foe. Front Physiol 6:96. https://doi.org/10.3389/fphys.2015.00096
2. Alwabari M et al (2023) Can non-invasive spectrophotometric hemoglobin replace laboratory hemoglobin concentrations for pre-operative anemia screening? A Diagnostic Test Accuracy Study. J Clin Med 12(17):5733. https://doi.org/10.3390/jcm12175733
3. Li S et al (2023) Electrochemical biosensors for whole blood analysis: recent progress, challenges, and future perspectives. Chem Rev 123(12):7953–8039. https://doi.org/10.1021/acs.chemrev.1c00759
4. Wekalao J et al (2023) Graphene-based THz surface plasmon resonance biosensor for hemoglobin detection applicable in forensic science. Plasmonics. https://doi.org/10.1007/s11468-023-02146-8
5. Wekalao J, Mandela N, Muheki J, Zaid A (2024) Design and analysis of a terahertz metasurface - based refractive index sensor for hemoglobin detection with behaviour prediction using polynomial regression. Plasmonics, no. 123456789. https://doi.org/10.1007/s11468-024-02445-8.
6. Naresh V, Lee N (2021) A review on biosensors and recent development of nanostructured materials-enabled biosensors. Sensors (Switzerland) 21(4):1–35. https://doi.org/10.3390/s21041109
7. Kulkarni MB, Ayachit NH, Aminabhavi TM (2022) Biosensors and microfluidic biosensors: from fabrication to application. Biosensors 12(7):543. https://doi.org/10.3390/bios12070543
8. Haleem A, Javaid M, Singh RP, Suman R, Rab S (2021) Biosensors applications in medical field: a brief review. Sens Int 2:100100. https://doi.org/10.1016/j.sintl.2021.100100
9. Singh AK, Mittal S, Das M, Saharia A, Tiwari M (2023) Optical biosensors: a decade in review. Alex Eng J 67:673–691. https://doi.org/10.1016/j.aej.2022.12.040
10. Uygun ZO (2023) Fundamentals of biological recognition elements. In: Fundamentals of Sensor Technology: Principles and Novel Designs 45–62. https://doi.org/10.1016/B978-0-323-88431-0.00017-X.
11. Chadha U et al (2022) Recent progress and growth in biosensors technology: a critical review. J Ind Eng Chem 109:21–51. https://doi.org/10.1016/j.jiec.2022.02.010
12. Cesewski E, Johnson BN (2020) Electrochemical biosensors for pathogen detection. Biosens Bioelectron 159:112214. https://doi.org/10.1016/j.bios.2020.112214
13 Kaur B, Kumar S, Kaushik BK (2023) Novel wearable optical sensors for vital health monitoring systems—a review. Biosensors 13(2):181. https://doi.org/10.3390/bios13020181
14. Fairuz Omar A (2013) Fiber optic sensors: an introduction for engineers and scientists. Sens Rev 33(2). https://doi.org/10.1108/sr.2013.08733baa.010.
15 Lininger A et al (2023) Chirality in light–matter interaction. Adv Mater 35(34):2107325. https://doi.org/10.1002/adma.202107325
16. Patel SK, Wekalao J, Mandela N, Al-Zahrani FA (2024) Design of encoded graphene-gold metasurface-based circular ring and square sensors for brain tumor detection and optimization using XGBoost algorithm. Diam Relat Mater 148:111439. https://doi.org/10.1016/j.diamond.2024.111439
17. Yahya AM, Salim ET, Hassan AI, Addie AJ (2023) Ag@graphene hybrid plasmonic nanocomposites by spray pyrolysis: synthesis, characterization and improved properties. J Opt. https://doi.org/10.1007/s12596-023-01467-5
18 Shah M, AlidoustGhatar A, Hayat A, Akhavan O, Jahani D (2023) Surface plasmon resonances in anisotropic strained graphene. J Opt Soc Am B 40(9):2315. https://doi.org/10.1364/josab.494514
19. Wekalao J, Alsalman O, Patel H, Manvani R, Patel SK (2024) Swift detection of heavy metals in water by encoded graphene–gold-metasurface sensor. Opt Quantum Electron 56(7):1199. https://doi.org/10.1007/s11082-024-07140-w
20 Xiao X, Zhang Y, Zhou L, Li B, Gu L (2022) Photoluminescence and fluorescence quenching of graphene oxide: a review. Nanomaterials 12(14):2444. https://doi.org/10.3390/nano12142444
21. Long Y-T, Jing C (2014) Localized surface plasmon resonance based nanobiosensors. Springer Berlin Heidelberg
22. Wen C, Wang L, Liu L, Shen XC, Chen H (2022) Surface-enhanced Raman probes based on gold nanomaterials for in vivo diagnosis and imaging. Chem Asian J 17(7):e202200014. https://doi.org/10.1002/asia.202200014
23 Zhang XF, Liu ZG, Shen W, Gurunathan S (2016) Silver nanoparticles: synthesis, characterization, properties, applications, and therapeutic approaches. Int J Mol Sci 17(9):1534. https://doi.org/10.3390/ijms17091534
24. Aliqab K, Wekalao J, Alsharari M, Armghan A, Agravat D, Patel SK (2023) Designing a graphene metasurface organic material sensor for detection of organic compounds in wastewater. Biosensors 13(8):1806739. https://doi.org/10.3390/bios13080759
25. Wang AX, Kong X (2015) Review of recent progress of plasmonic materials and nano-structures for surface-enhanced raman scattering. Materials 8(6):3024–3052. https://doi.org/10.3390/ma8063024
26. Langer J et al (2020) Present and future of surface-enhanced Raman scattering. ACS Nano 14(1):28–117. https://doi.org/10.1021/acsnano.9b04224
27 Aliqab K, Wekalao J, Alsharari M, Armghan A, Agravat D, Patel SK (2023) Designing a graphene metasurface organic material sensor for detection of organic compounds in wastewater. Biosensors 13(8):759. https://doi.org/10.3390/bios13080759
28. Almawgani AHM, Wekalao J, Patel SK, Alzahrani A, Gumaih HS, Armghan A (2024) Optimization of graphene-based square slotted surface plasmon resonance refractive index biosensor for accurate detection of pregnancy. Plasmonics. https://doi.org/10.1007/s11468-024-02290-9.
29. A. H. M. Almawgani, J. Wekalao, S. K. Patel, A. Alzahrani, and H. S. Gumaih, 2024 "Design and development of a split ring resonator and circular disc metasurface based graphene / gold surface plasmon resonance sensor for illicit drugs detection," *Plasmonics* 123456789 https://doi.org/10.1007/s11468-024-02306-4.
30. Wekalao J, AKU, Albargi HB, Jalalah M, Almawgani AHM, Armghan A (2024) Graphene and gold metasurface-based terahertz surface plasmon resonance sensor for explosive detection. *Plasmonics*. https://doi.org/10.1007/s11468-024-02229-0.

31. Wekalao J, Albargi HB, Patel SK, Jalalah M, Almawgani AHM (2024) Terahertz optical ultrasensitive glucose detection using graphene and silver surface plasmon resonance metasurfaces for biomedical applications. *Plasmonics*, no. 123456789. https://doi.org/10.1007/s11468-024-02278-5.
32. Patel SK, Alsalman O, Taya SA, Parmar J (2023) Skin cancer detection using tunable graphene SPR optical sensor designed using circular ring resonator. Plasmonics. https://doi.org/10.1007/s11468-023-01957-z
33. Wekalao J, Alsalman O, Shobhit RM (2024) Graphene biosensor design based on glass substrate for forensic detection of illicit drugs. Opt Quantum Electron. https://doi.org/10.1007/s11082-024-06690-3
34. Muheki J, Wekalao J, Albargi HB, Jalalah M, Almawgani AHM (2024) A graphene gold metasurface inspired surface plasmon resonance sensor designed for terahertz applications in sensing and detection of heavy metals in water.
35. Patel SK, Wekalao J, Albargi HB, Jalalah M, AHM Almawgani (2024) Design and simulation of metasurface - enhanced graphene biosensors for cancer biomarker detection. Plasmonics, no. 123456789. https://doi.org/10.1007/s11468-024-02224-5.
36. Alsalman O, Wekalao J, Arun Kumar U, Agravat D, Parmar J, Patel SK (2023) Design of split ring resonator graphene metasurface sensor for efficient detection of brain tumor. Plasmonics, no. 123456789. https://doi.org/10.1007/s11468-023-02002-9.
37. Patel SK, Wekalao J, Alsalman O, Surve J, Parmar J, Taya SA (2023) Development of surface plasmon resonance sensor with enhanced sensitivity for low refractive index detection. Opt Quantum Electron 55(11):1001. https://doi.org/10.1007/s11082-023-05265-y
38. Wekalao J, Patel SK, Alsalman O, Surve J, Anushkannan NK, Parmar J (2023) Waterborne bacteria detecting highly sensitive graphene metasurface based cost-efficient and efficient refractive index sensors. Plasmonics 19(1):347–61
39. Aliqab K, Wekalao J, Alsharari M, Armghan A, Agravat D, Patel SK (2023) Designing a graphene metasurface organic material sensor for detection of organic compounds in wastewater. Biosensors 13(8):1–16. https://doi.org/10.3390/bios13080759
40 Wekalao J, Alsalman O, Natraj NA, Surve J, Parmar J, Patel SK (2023) Design of graphene metasurface sensor for efficient detection of COVID-19. Plasmonics 18(6):2335–45. https://doi.org/10.1007/s11468-023-01946-2
41. Wekalao J, Patel SK, Anushkannan NK, Alsalman O, Surve J, Parmar J (2023) Design of ring and cross shaped graphene metasurface sensor for efficient detection of malaria and 2 bit encoding applications. Diam Relat Mater 139:110401. https://doi.org/10.1016/j.diamond.2023.110401
42 Hma Salah N (2023) Sensitivity enhancement of the surface plasmon resonance–based gas sensing by few layers of black phosphorus. Plasmonics 18(6):2225–2233. https://doi.org/10.1007/s11468-023-01951-5
43. Anushkannan NK, Wekalao J, Patel SK, Al-Zahrani FA (2024) Design of encoded and tunable graphene-gold metasurface-based surface plasmon resonance sensors for glucose detection in the terahertz regime. Plasmonics, no. 123456789. https://doi.org/10.1007/s11468-024-02452-9.
44 Ben Soltane I, Dierick F, Stout B, Bonod N (2024) Generalized Drude-Lorentz model complying with the singularity expansion method. Adv Opt Mater 12(12):2400093. https://doi.org/10.1002/adom.202400093
45. Patel SK, Parmar J, Katkar V (2022) Ultra-broadband, wide-angle plus-shape slotted metamaterial solar absorber design with absorption forecasting using machine learning. Sci Rep 12(1):1–14. https://doi.org/10.1038/s41598-022-14509-y
46. Alsaif H et al. (2024) Design and optimization of a MXene-based terahertz surface plasmon resonance sensor for malaria detection. Plasmonics, no. 123456789. https://doi.org/10.1007/s11468-024-02455-6.
47. Twayana K, Rebolledo-Salgado I, Deriushkina E, Schröder J, Karlsson M, Torres-Company V (2022) Spectral interferometry with frequency combs. Micromachines 13(4). https://doi.org/10.3390/mi13040614.
48. Li L, Lei J, Wu L, Pan F (2021) Spectroscopic ellipsometry. In Handbook of Modern Coating Technologies: Advanced Characterization Methods, pp. 45–83. https://doi.org/10.1016/B978-0-444-63239-5.00002-0.
49. Surve J, Jadeja R, Parmar T, Parmar J, Parmar J (2022) A terahertz-based graphene metasurface sensor for hemoglobin detection with high Q factor and low figure of merit. In: Terahertz Devices, Circuits and Systems: Materials, Methods and Applications, pp. 41–51. https://doi.org/10.1007/978-981-19-4105-4_3.
50. SC, Trupti Kamani TS, Patel SK, Anushkannan NK, Khalifa SB (2024) Design and development of surface plasmon resonance biosensor for early detection of cervical cancer utilizing nucleus and cytoplasm. Pasmonics
51. Saadatmand B, Haji Najafi Chemerkouh MJ, Ahmadi V, Hamidi SM (2023) Graphene-based integrated plasmonic sensor with application in biomolecule detection. J Opt Soc Am B 40(1):1. https://doi.org/10.1364/josab.472734
52. Nashaat D, Elsadek HA, Abdallah E, Elhenawy H, Iskander MF, Communication A (2009) Using metamaterial structures. Technology 1:7–10
53. Patel SK et al (2022) Encoding and tuning of THz metasurface-based refractive index sensor with behavior prediction using XGBoost regressor. IEEE Access 10:24797–24814. https://doi.org/10.1109/ACCESS.2022.3154386
54. Saadatmand SB, Chemerkouh MJHN, Ahmadi V, Hamidi SM (2023) Design and analysis of highly sensitive plasmonic sensor based on 2-D inorganic Ti-MXene and SrTiO3interlayer. IEEE Sens J 23(12):12727–12735. https://doi.org/10.1109/JSEN.2023.3270133
55. Mohammad Javad Haji Najafi Chemerkouh MH, Seyedeh Bita Saadatmand (2022) Ultra-high-sensitive biosensor based on SrTiO3 and two-dimensional materials: ellipsometric concepts. Opt Mater Express 7
56. Tombe R, Viriri S (2022) Effective processing of convolutional neural networks for computer vision: a tutorial and survey. IETE Tech Rev (Institution of Electronics and Telecommunication Engineers, India) 39(1):49-62. https://doi.org/10.1080/02564602.2020.1823252
57. Cordeiro JR, Raimundo A, Postolache O, Sebastião P, (2021) Neural architecture search for 1d cnns Different approaches tests and measurements. Sensors 21(23). https://doi.org/10.3390/s21237990.
58. Parmar J, Patel SK, Katkar V (2022) Graphene-based metasurface solar absorber design with absorption prediction using machine learning. Sci Rep 12(1):2609. https://doi.org/10.1038/s41598-022-06687-6
59. Babu GS, Zhao P, Li XL (2016) Deep convolutional neural network based regression approach for estimation of remaining useful life. In: Lecture Notes in Computer Science (including subseries Lecture Notes in Artificial Intelligence and Lecture Notes in Bioinformatics), pp. 214–228. https://doi.org/10.1007/978-3-319-32025-0_14.
60. Wang X et al (2021) Deep spatiotemporal convolutional-neural-network-based remaining useful life estimation of bearings Chinese J Mech Eng (English Ed. 34(1). https://doi.org/10.1186/s10033-021-00576-1.
61. Babu GS, Zhao P, Li X (2016) Deep convolutional neural network based regression approach for estimation. In: Database Systems for Advanced Applications: 21st International Conference, DASFAA 2016 Dallas, TX, USA, April 16–19, 2016 Proceedings, Part I, pp. 214–228.

62. Learning D (2016) Deep Learning - Goodfellow. Nature 26(7553):436
63. Nair V, Hinton GE (2010) Rectified linear units improve restricted Boltzmann machines. In: ICML 2010 - Proceedings, 27th International Conference on Machine Learning, 2010, pp. 807–814.
64. Ioffe S, Szegedy C (2015) Batch normalization: accelerating deep network training by reducing internal covariate shift. In: 32nd International Conference on Machine Learning, ICML 2015, pp. 448–456.
65. Srivastava N, Hinton G, Krizhevsky A, Sutskever I, Salakhutdinov R (2014) Dropout: a simple way to prevent neural networks from overfitting. J Mach Learn Res 15:1929–1958
66. Bishop CM, Nasrabadi NM (2006) Pattern recognition and machine learning. New York: Springer. https://doi.org/10.1117/1.2819119

Publisher's Note Springer Nature remains neutral with regard to jurisdictional claims in published maps and institutional affiliations.

Springer Nature or its licensor (e.g. a society or other partner) holds exclusive rights to this article under a publishing agreement with the author(s) or other rightsholder(s); author self-archiving of the accepted manuscript version of this article is solely governed by the terms of such publishing agreement and applicable law.